T H E U N I V E R S I T Y O F T U L S A

THE GRADUATE SCHOOL

A FULLY COUPLED GEOMECHANICS AND MULTIPHASE FLOW AND TRANSPORT SIMULATION MODEL FOR NATURALLY AND HYDRAULICALLY FRACTURED RESERVOIRS

by
Guotong Ren

A thesis submitted in partial fulfillment of

the requirements for the degree of Master of Science

in the Discipline of Petroleum Engineering

The Graduate School

The University of Tulsa

2016

T H E U N I V E R S I T Y O F T U L S A

THE GRADUATE SCHOOL

A FULLY COUPLED GEOMECHANICS AND MULTIPHASE FLOW AND TRANSPORT SIMULATION MODEL FOR NATURALLY AND HYDRAULICALLY FRACTURED RESERVOIRS

by
Guotong Ren

A THESIS

APPROVED FOR THE DISCIPLINE OF

PETROLEUM ENGINEERING

By Thesis Committee

_____, Chair
Rami M Younis

_____
Albert C. Reynolds

_____
Michael Keller

COPYRIGHT STATEMENT

ABSTRACT

Guotong Ren (Master of Science in Petroleum Engineering),

A fully coupled geomechanics and multiphase flow and transport simulation model for naturally and hydraulically fractured reservoirs

Directed by Rami Younis

72, pp., Chapter 5: Conclusions

(309 words)

Unconventional reservoirs are typically comprised of a multicontinuum stimulated formation, with complex fracture networks that have a wide range of length scales and geometries. While hydraulic fractures may be propped with a varying concentration field of proppant, natural fractures are predominantly supported by pore pressure. A timely topic in the simulation of unconventional petroleum resources is in coupling the geomechanics of the fractured media to multiphase fluid flow and transport. This coupling is paramount towards the basic understanding of a number of important practical questions such as what causes the sudden loss of productivity in wells when neighboring wells are completed?

To adequately capture the effects of the multiscaled fracture system in terms of both flow and geomechanics, we develop a mixed approach that fully couples an extended finite element method (XFEM)) to a hybrid multiphase flow model that couples an embedded-discrete-fracture model (EDFM) with multiple interacting continua (MINC).

This optimized model can reduce the computational cost that is associated with the widely applied unstructured mesh approaches; A Cartesian mesh is used and the two

numerical methods share this single conformal rectangular grid with embedded fractures for both mechanical deformation and fluid-flow problems. Owing to the hybrid continuum-type models, a highly refined mesh is not necessary in order to obtain accurate strain/stress and pressure fields. The MINC concept allows the hybrid model to handle the extreme contrast in conductivity between the small-scale fracture network and the ultratight matrix that results in steep potential gradients.

The strain-stress relationship in multi porosity media is used as a constitutive equation for coupling flow and rock mechanics. Moreover, assuming proppant preexists in the system, a proppant model is proposed to consider the influence on fracture aperture.

We validate the accuracy of our approach using Mandle's Problem and a pure mechanics single fracture problem. We present simulation results for scenarios with multiple fractures.

ACKNOWLEDGEMENTS

First and foremost, I would like to express my sincere thanks to my adviser, Dr. Rami Younis, who has guided me through the years. During my study at TU, I have benefited tremendously from his thoughtful guidance and insightful suggestions. Dr. Younis has been a consistent source of knowledge, advice and encouragement, not only to my research work, but also to my personal life.

I would also like to thank other members of my dissertation committee, Dr. Albert C. Reynolds and Dr. Michael Keller for their time and effort to serve on my committee and review my dissertation.

I owe my gratitude to the Department of Petroleum Engineering, all the faculty, staff, and my fellow students. They made my years at TU inspiring and rewarding. Their great help and friendship are very much appreciated.

I would like to express my deepest gratitude to my parents for their endless love, support, and encouragement throughout my graduate study at TU. My achievements would not have been possible without their help and inspiration.

TABLE OF CONTENTS

LIST OF FIGURES

LIST OF TABLES

CHAPTER 1.

INTRODUCTION

1.1 Literature Review

Reservoir geomechanics plays an important role in analyzing phenomena, such as subsidence, primary compaction drive, hydro fracturing, and wellbore stability and Quantification of the state of deformation and stress of the reservoir is essential for correct prediction of these phenomena (Jha and Juanes, 2007). Numerous studies have been taken on coupled flow and geomechanics simulation of conventional (unfractured) reservoir (Tran et al., 2002; Thomas et al. 2002; Chin et al., 1998; Jha and Juanes, 2007). In the past decade, unconventional reservoirs has become increasingly an important oil and gas resources in the United States. Unconventional reservoirs are comprised of an ultra-low permeability fractured matrix that may consist of multiple continua. Natural fractures form highly connected networks with a wide range of length scales. The fractures are primarily supported by pore pressure. Horizontal wells stimulated by hydraulic fractures that emanate from the wellbore along clusters within multiple stages. The fractures are supported by pore pressure as well as proppants that are delivered during the completions process. Empirical observations from field practice suggest that geomechanical effects may play a first-order role in production form unconventional reservoirs. It is frequently observed that the production rate in tight gas reservoirs declines rapidly in a manner that is believed to be closely related to the evolution of fracture aperture and permeability with

time (Huang and Ghassemi, 2012). Therefore, it is necessary and essential to develop a coupled flow and geomechanics simulator that can capture the influence of rock deformation and fracture aperture changes on field properties such as porosity and permeability.

The fundamental of geomechanics are constructed on the concept of effective stress formulated by Terzaghi and Biot (Biot, 1941; Skempton, 1960). Terzaghi first proposed the relationship for effective stress for one dimensional case (Skempton, 1960). Later, Biot gave the quasi-static constitutive equations relate the strain tensor linearly to both the stress tensor (Berryman and Wang, 1995). and the fluid pressure and developed a generalized theory of 3D consolidation. However, in the reservoir where fractures are present, Biot poroelastic theory of single porosity is no longer applicable. Therefore, in order to characterize flow and deformation in the fractured reservoir, Barenblatt et al first introduced the dual-porosity/dual-permeability concept. In dual porosity theory, rock and fracture are represented by two different interacting continua blocks. Typically, rock continua is entirely surrounded by a thin layer of fracture continua. Since then dual porosity model got investigated by many researchers. Bai (1999) offered a more rigorous physical interpretation of dual porosity poroelastic (DPP). Two separate effective stress laws are applied in order to capture different extent of deformation of matrix and fractures. Berryman and Wang **(**1995) proposed a set of physical experiments to interpret the linear constitutive parameters in dual porosity model. Later Berryman (2002) determined those parameters through a more elegant fashion by using a new self-similar thought experiment. Kim extended dual porosity model from Berryman to multiple interacting continua method (MINC) by using the same idea of self-similar thought experiment to determine

coefficients of multiple porosity systems (Kim, 2012). Kim applied MINC idea to simulating fluid flow with chemical reaction in the fractured geothermal reservoir (Kim, 2015). Another dual continuum concept, dual permeability method has been used for the coupled flow and geomechanics. (Huang and Ghassemi 2012; Wei and Zhang; 2010). The existing dual porosity approaches average fractures out and lose fracture information such as length, orientation and aperture.

Another category of coupled flow and geomechanics method treats fracture explicitly. A vast literature is available on a number of numerical approach for explicitly dealing with fracture in coupled flow and geomechanics. Among all of these methods, fracture is expressed in a lower dimension. For example, if studied domain is three dimension, the fractures are described as 2D faces. Some researchers (Levonyan, 2011; Monteagudo et al., 2011; Garipov et al., 2014) employ a discrete fracture model (DFM) (Karimi-Fard et al., 2003) for flow model, in which a single static unstructured grid represents all the fractures as low-dimensional objects embedded within the matrix deformation. In order to describe poromechanics deformation, they duplicate nodes on the fracture (element interface) because addition degree of freedoms are needed. A good mesh generator which can handle very complicated geometry is a prerequisite. And it is only suitable to the problem where fractures are static. Otherwise, remesh and complicated post processing would be needed. Another semi-analytical method for fracture mechanics called boundary element method (BEM) or displacement discontinuity method (DDM) is widely used in coupled flow and geomechanics simulation. DDM, a special BEM was developed by Crouch (1976) and designed for handling problems with crack-like geometries. Wu (2015) applied the DDM on hydraulic fractures and horizontal wells. However, she

assumed fractures are embedded in an elastic domain and flow only occurs in fractures. McClure and Horne (2010) used DFM for flow and DDM for mechanics to simulate natural fracture reservoirs. Even though they considered flow in porous medium and its interaction between rock matrix and fractures, it is assumed that fracture deformation does not affect matrix fluid pressure and changes in matrix fluid pressure do not affect stress on fractures (McClure, 2015). Ganis et al. (2013) utilized symmetric Galerkin boundary element method (SGBEM) coupled with finite element method to capture deformation of porous media. Nevertheless, the error of this method is small only when domain size is large and fractures are not close to the boundary. A variational approach, phase-field method, to solving fracture problems recently is proposed. For example, Bourdin et al. (2012) formulated phase field in elasticity for hydraulic cracks. Later, Singh (2014) and Wick et al. (2015) extended the elasticity to poroelastic nature of the reservoir rock and used phase-field method to study linear fracture propagation. With a phase-field approach, a lower-dimensional crack surface is approximated as a diffusive transition zone characterized by a band width 2ε, by a phase-field function φ (Wick et al., 2015). Phase-field method avoids relying on mesh generator and is able to handle complex fracture pattern. Recent years, extended finite element method (XFEM) (Moës et al., 1999, Belytschko, 2001) has been successfully implemented on the linear elastic fracture mechanics and its propagation. XFEM doesn't need fracture to be aligned with grids and can achieve good precision without requiring a highly refined mesh. Later on, Lamb et al. (2010) developed a model that coupled XFEM with dual permeability method for poroelastic medium.

In this thesis, a fully coupled XFEM-EDFM with dual porosity hybrid model is presented to accurately simulate fields of displacement and stress and fluid flow in

fractured reservoirs. EDFM is used to describe the fluid flow interaction between the porous matrix and primary fractures, while XFEM is used to address the discontinuous displacement field within elements which intersect fractures. . The dual porosity concept allows the hybrid model to handle the small-scale fracture network around primary fractures in SRV. The proposed hybrid method includes the effect of each hydraulic fractures explicitly without requiring the simulation mesh to conform to the fracture geometry and also avoids to explicitly represent natural fracture networks. Thus the challenges of high computational cost and the requirement for complex meshing technique associated with UDFM are overcome. The existing studies in the literature did not consider the effect of proppant. We propose a proppant model to simulate production from hydraulic fractures. In contrast, we consider that natural fractures are predominantly supported by pore pressure. The coupled system of nonlinear equations, boundary conditions and associated constitutive relations are solved by the Newton's method using a fully-implicit formulation to ensure solution stability.

1.2 Outline

The thesis is organized as follows:

1. In Chapter 2, the theory of linear fracture elastic fracture mechanics is explained. A governing equation for poromechanics deformation is described. Then we introduce dual porosity model to capture the deformation of fine-scale natural fractures. An extended finite element method combined with proppant model is also proposed to precisely predict the hydraulic fracture (prime fractures) aperture change and the proppant deformation in hydraulic fractures. At the end of this chapter, weak form of the governing equation and finite element discretization are described.

2. In Chapter 3, we first introduce the governing equations for fluid flow. Then the EDFM and dual porosity model are described. Next, Discretization of the EDFM and dual porosity model for fluid flow is formulated. The solution algorithm for solving the coupled system is explained in the end.

3. In Chapter 4, we verify our model by analytical solutions. And we analyze the impact of dual porosity and proppant mechanics property on production.

4. Chapter 5 concludes the .thesis with accomplishments and recommendations for future work.

CHAPTER 2

POROMECHANICS DEFORMATION

The objective of this chapter is to develop the weak form of the coupled XFEM-dual porosity with proppant model and use the Galerkin method to formulate discretization of the weak form.

2.1 Theory of Linear Elastic Fracture Mechanics

Linear elastic theory predicts that stress at the tip of the crack tends to be infinite. Griffith (1921) first formulated a crack propagation criterion for brittle materials. He succeeded in finding the relationship between crack size and fracture strength. Later in the middle 1950s, Irwin modified Griffith theory and introduced the concept of stress intensity factor (SIF) and energy release rate. Westergaard (1939) proposed an airy function as a solution to the crack problem in 2D.

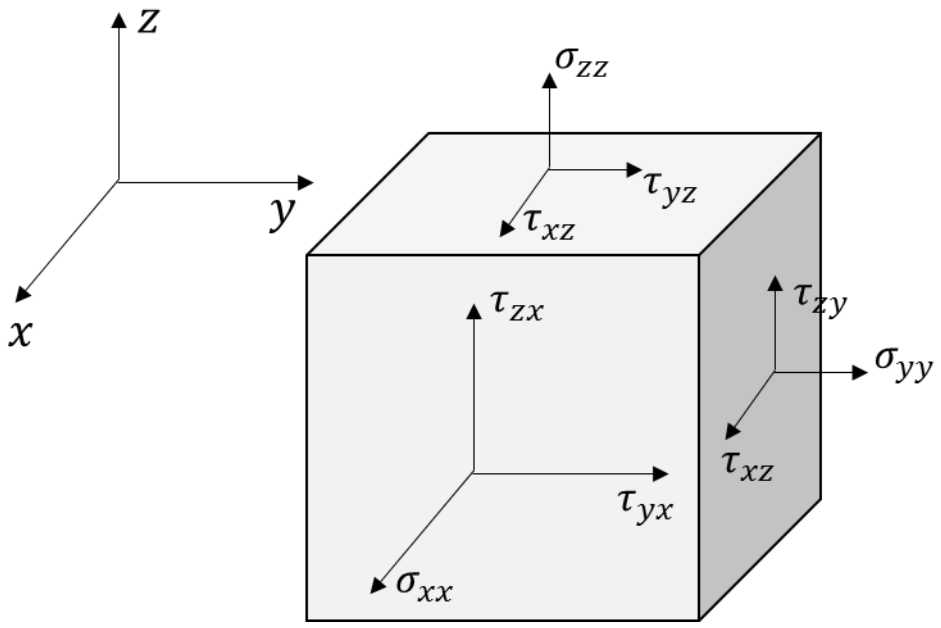

Figure 2.1 stress components on an infinitesimal material element

Fig. 2.1 Next, we will first introduce the equilibrium equations of stress. From Fig. 2.1, the equation for equilibrium in x direction can be written as

$$\left(\sigma_x + \frac{\partial \sigma_x}{\partial x} dx\right) dydz - \sigma_x dydz + \left(\tau_{xy} + \frac{\partial \tau_{xy}}{\partial y} dy\right) dzdx - \tau_{xy} dxdz +$$

$$\left(\tau_{xz} + \frac{\partial \tau_{xz}}{\partial z} dz\right) dxdy - \tau_{xy} dxdy = 0 \qquad (2.1)$$

We can write the similar forms in y and z direction. And these three equations from stress equilibrium equation under quasi-static state are the follows:

$$\frac{\partial \sigma_x}{\partial x} + \frac{\partial \tau_{xy}}{\partial y} + \frac{\partial \tau_{xz}}{\partial z} = 0 \qquad (2.2a)$$

$$\frac{\partial \sigma_y}{\partial y} + \frac{\partial \tau_{yz}}{\partial z} + \frac{\partial \tau_{xy}}{\partial x} = 0 \qquad (2.2b)$$

$$\frac{\partial \sigma_z}{\partial z} + \frac{\partial \tau_{zx}}{\partial x} + \frac{\partial \tau_{zy}}{\partial y} = 0 \qquad (2.2c)$$

In two dimensional case, Eq. (2.2) could be reduced to

$$\frac{\partial \sigma_x}{\partial x} + \frac{\partial \tau_{xy}}{\partial y} = 0 \qquad (2.3a)$$

$$\frac{\partial \sigma_y}{\partial y} + \frac{\partial \tau_{xy}}{\partial x} = 0 \tag{2.3b}$$

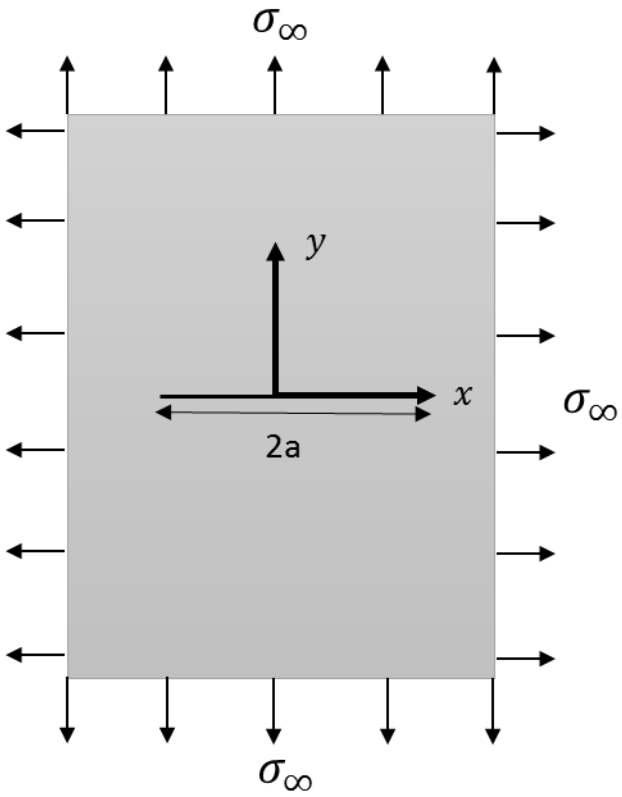

Figure 2.2 A biaxially loaded infinite plate containing a crack

Now, we can solve the problem of biaxially loaded plate with a central crack in **Fig. 2.2** The governing equation is the Eq. (2.3) , boundary conditions are given as follows

$$\sigma_y = 0 \text{ for } -a < x < +a \text{ and } y = 0 \tag{2.4}$$

$$\sigma_x = \sigma_\infty \text{ and } \sigma_y = \sigma_\infty \text{ for } x \to \pm\infty \text{ and } y \to \pm\infty \tag{2.5}$$

$$\sigma_y = \infty \text{ for } x = \pm a \text{ and } y = 0 \tag{2.6}$$

Westergaard introduced a specific type of Airy stress function Φ using an analytic complex stress function $\phi(z)$ of which the first and second order integrals are assumed to exist:

$$\Phi = \mathrm{Re}\bar{\bar{\phi}}(z) + y \cdot \mathrm{Im}\bar{\phi}(z) \tag{2.7}$$

Where $\bar{\phi}(z), \bar{\bar{\phi}} =$ first and second order integrals of $\phi(z)$ respectively and $z = x + i \cdot y$.

Airy stress functions give us

$$\sigma_x = \frac{\partial^2 \Phi}{\partial y^2}, \sigma_y = \frac{\partial^2 \Phi}{\partial y^2}, \tau_{xy} = -\frac{\partial^2 \Phi}{\partial x \partial y} \tag{2.8}$$

And if we plug Eq. (2.7) into Eq. (2.8), we can get the expressions for stress.

$$\sigma_x = \mathrm{Re}\phi(z) - y \cdot \mathrm{Im}\phi'(z) \tag{2.9}$$

$$\sigma_x = \mathrm{Re}\phi(z) + y \cdot \mathrm{Im}\phi'(z) \tag{2.10}$$

$$\tau_{xy} = -y \cdot \mathrm{Re}\phi'(z) \tag{2.11}$$

In the region near the crack tip, the solution above can be simplified into the following form:

$$\sigma_x = \frac{\sigma\sqrt{\pi a}}{\sqrt{2\pi r}} \cos\frac{\theta}{2}\left(1 - \sin\frac{\theta}{2}\sin\frac{3\theta}{2}\right) \tag{2.12}$$

$$\sigma_y = \frac{\sigma\sqrt{\pi a}}{\sqrt{2\pi r}} \cos\frac{\theta}{2}\left(1 + \sin\frac{\theta}{2}\sin\frac{3\theta}{2}\right) \tag{2.13}$$

$$\tau_{xy} = \frac{\sigma\sqrt{\pi a}}{\sqrt{2\pi r}} \sin\frac{\theta}{2}\cos\frac{\theta}{2}\cos\frac{3\theta}{2} \tag{2.14}$$

Where r, θ consist of the local polar system located at the crack tip. In the **Fig. 2.3**, it shows the polar system at the crack tip.

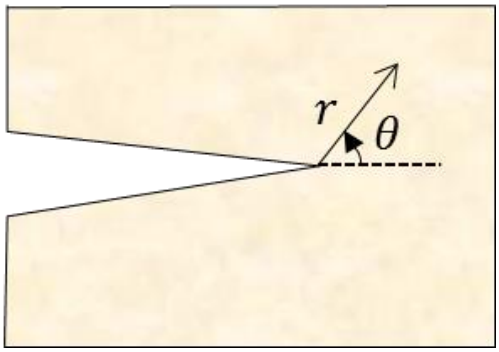

Figure 2.3 The polar coordinate system associated with the crack tip

A function ϕ that satisfies equilibrium equations and boundary conditions is given as the following:

$$\phi = \frac{\sigma_\infty}{\sqrt{1-\frac{a^2}{z^2}}} \tag{2.15}$$

Where a is the half crack length.

We can also get a useful expression of crack opening displacement for 2D domain.

$$\mathrm{COD} = \frac{2\sigma_\infty}{E'}\sqrt{a^2 - x^2} \tag{2.16}$$

Where $E' = E$ in the plane stress condtion, $E' = \frac{E}{1-\nu^2}$ in the plane strain condition. E, ν are the Young's modulus and Poisson's ratio respectively.

2.2 Force Equilibrium Equation

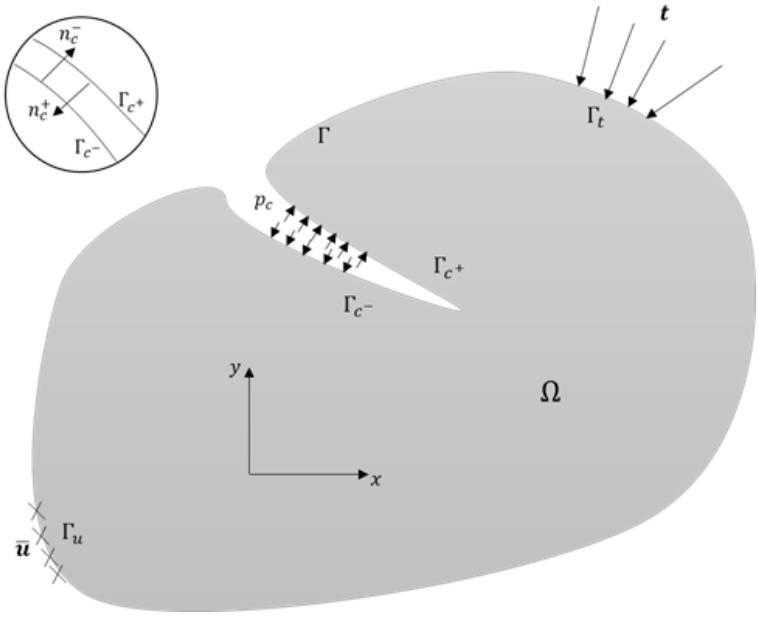

Figure 2.4. A body in a state of elastostatic equilibrium

Fig. 2.4 shows a body with a fracture under equilibrium state. $\boldsymbol{n}_t$ is the unit outward normal vector to the external boundary, $\boldsymbol{t}$ is the prescribed traction applied on the boundary, $\bar{\boldsymbol{u}}$ is prescribed displacement on the external boundary. On the inner fracture boundary Γ_c, fracture pore pressure p_c is exerted on fracture inner faces. The two unit outer normal vectors on two fracture faces are $\boldsymbol{n}_c^+$ and $\boldsymbol{n}_c^-$.

The governing equation for poromechanics under quasi-static assumption is:

$$\nabla \cdot \boldsymbol{\sigma} + \rho_b \boldsymbol{g} = 0 \tag{2.17}$$

Where $\boldsymbol{\sigma}$ is Cauchy total stress tensor and ρ_b is the bulk density.

The boundary conditions are given as:

$$\boldsymbol{\sigma} \cdot \boldsymbol{n}_t = \boldsymbol{t} \text{ on } \Gamma_t \tag{2.18a}$$

$$\boldsymbol{u} = \bar{\boldsymbol{u}} \quad \text{on } \Gamma_u \tag{2.18b}$$

$$\boldsymbol{\sigma} \cdot \boldsymbol{n}_c^- = -\boldsymbol{\sigma} \cdot \boldsymbol{n}_c^+ = -p_c \boldsymbol{n}_c^+ = p_c \boldsymbol{n}_c^- = p_c \boldsymbol{n}_c = \bar{\boldsymbol{p}} \text{ on } \Gamma_c \tag{2.18c}$$

Here we assume the infinitesimal transformation, from which the strain tensor defined as the symmetric gradient of the displacement

$$\boldsymbol{\varepsilon} = \frac{1}{2}(\nabla \boldsymbol{u} + \nabla^T \boldsymbol{u}) \tag{2.19}$$

And the volume strain $\epsilon_v = trace(\boldsymbol{\varepsilon})$.

2.3 Dual Porosity

Natural fractures near hydraulic fractures have a significant impact on increasing the mobility of fluid in the reservoir. However, treating complicated natural fracture pattern explicitly by EDFM and XFEM is difficult and also causes expensive computational cost. In characterizing flow and deformation between matrix and fractures, an extension from single porosity (Biot, 1957) to dual porosity concept (Barenblatt, 1960) is applied to address the problem. DPP provided by Bai (1999) which has a rigorous physical interpretations of dual porosity model is implemented in the simulator.

In Bai's model, instead of using only one effective stress law (Wilson and Aifantis, 1982), two separate effective stress laws for fracture and matrix are assumed as follows:

$$\boldsymbol{\sigma}_m = \boldsymbol{\sigma}'_m - \alpha_m p_m \boldsymbol{I} \tag{2.20a}$$

$$\boldsymbol{\sigma}_f = \boldsymbol{\sigma}'_f - \alpha_f p_f \boldsymbol{I} \tag{2.20b}$$

Where $\boldsymbol{\sigma}_m$ and $\boldsymbol{\sigma}_f$ are total stress for matrix and fracture separately. $\boldsymbol{\sigma}'_m$ and $\boldsymbol{\sigma}'_f$ are effective stress for matrix and fracture. α_m and α_f are Biot's coefficients for matrix and fracture and have a value between porosity and unity.

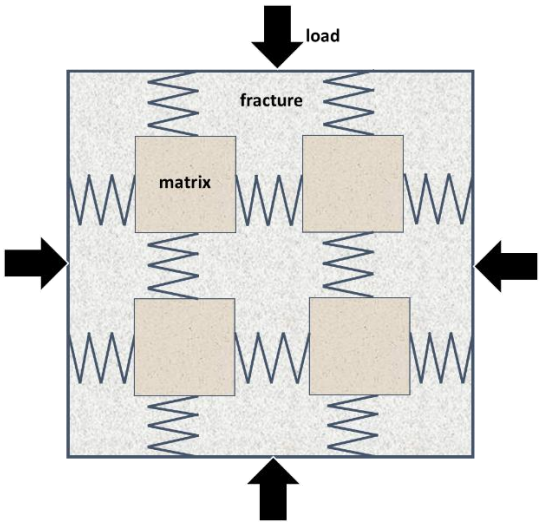

Figure 2.5. schematic dual porosity system

The relationship between matrix and fracture is shown in the **Fig. 2.5**. The model assumes matrix surrounded by orthogonal intersecting fracture. After deformation, total stresses in each continuum are kept equal,

$$\boldsymbol{\sigma} = \boldsymbol{\sigma}_m = \boldsymbol{\sigma}_f \tag{2.21}$$

Whereas, total strain are summed from those of two media.

$$\boldsymbol{\varepsilon} = \boldsymbol{\varepsilon}_m + \boldsymbol{\varepsilon}_f \tag{2.22}$$

From Eq. (2.20) to (2.22) and Hooke's Law, a modified effective stress law can be written as:

$$\boldsymbol{\sigma} = D_{mf} : \boldsymbol{\varepsilon} - D_{mf} : C_m : \alpha_m p_m \boldsymbol{I} - D_{mf} : C_f : \alpha_f p_f \boldsymbol{I} \tag{2.23}$$

Where D_{mf} is fourth order elastic stiffness tensor evaluated from property of matrix and fracture. C_m and C_f are compliance tensor for matrix and fracture. In this thesis, we assume linear elastic property for both matrix and fracture. C_m and C_f for the two dimensional case will be :

$$C_m = \frac{1}{E'}\begin{bmatrix} 1 & -v' & 0 \\ -v' & 1 & 0 \\ 0 & 0 & 1+v' \end{bmatrix} \tag{2.24}$$

Where $E' = E$ and $v' = v$ for plane stress, and $E' = \frac{E}{1-v^2}$ and $v' = \frac{v}{1-v}$ for plane strain.

$$C_f = \frac{1}{S}\begin{bmatrix} \frac{1}{K_n} & 0 & 0 \\ 0 & \frac{1}{K_n} & 0 \\ 0 & 0 & \frac{1}{K_{sh}} \end{bmatrix} \tag{2.25}$$

Where S is fracture spacing.

And for the convenience of derivation in the later part, we define the following variables:

$$\alpha_m^* = \alpha_m D_{mf} : C_m \tag{2.26a}$$

$$\alpha_f^* = \alpha_f D_{mf} : C_f \tag{2.26b}$$

The advantage of the model is that it includes two sets of parameters of matrix and fracture. Consequently it considers the matrix and fracture deformation individually. The Eq. (2.23) indicates that the integrated matrix and fracture system deforms in a same manner where ε is the total strain for the system. In the simulator, Eq. (2.23) is used as the effective stress law for dual porosity. After displacement fields are solved, strain for each continuum can be obtained from Eq. (2.20) to (2.22).

2.4 Proppant Model

Proppants in hydraulic fractures resist closure of fractures thus play a significant role in unconventional reservoir production. However, because of interaction between proppant and hydraulic surfaces, proppant may be deformed, embedded or crushed in the

fractures. Numerous experimental and analytical studies have investigated these three factors (deformation, embedment and crush) causing reduction in fracture conductivity and production. (Mindlin and Deresiewicz, 2013; Huitt and Mcglothlin, 1958; Huiit et al., 1959; Volk et al., 1981; Guo, 2008; Lacy et al., 1998; Li et al., 2015). We can get the following conclusions from the research mentioned above:

1. The condition of sand propping would crush rather than embed under the weight of overburden (Huiit et al., 1959)

2. Many factors such as rock property, proppant size and mechanical property, concentration of proppant-paving etc. could influence embedment of the proppant.

3. As the elastic modulus of coalbed (embedment surface) increases, the change in fracture aperture gradually approaches the proppant deformation, and the proppant embedment approaches zero. (Li et al., 2015)

Few research has investigated numerical analysis of proppant behaviors in hydraulic fractures. Here we propose a simple proppant model for hydraulic fractures. No conductivity lost caused by proppants is assumed and the proppant obeys linear elastic behaviors. We also consider elastic modulus of embedment surface is larger than that of proppant so that reduction in fracture aperture is mainly caused by proppant deformation. We define the force exerted on fracture faces by proppants as p_p.

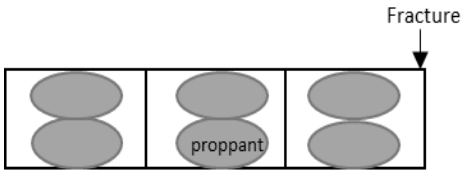

(a) Initial

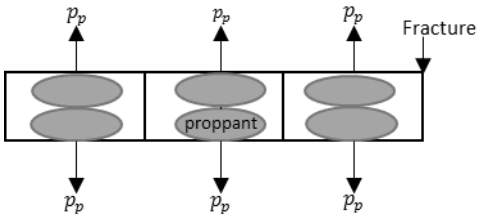

(b) Deformed

Figure 2.6 Initial and Deformed configuration
of propants in the discretized fracture (2D)

During production process, decrease of hydraulic fracture pressure causes a tendency of fracture closure. However, when proppant is present, deformed proppants will exert force on fracture faces and resist closure. According to the Hooke's Law, the pressure p_p caused by proppant will be

$$p_p = \begin{cases} E_p \frac{-\boldsymbol{w}\cdot\boldsymbol{n}_c}{D_i} & \boldsymbol{w}\cdot\boldsymbol{n}_c < \boldsymbol{0} \\ 0 & else \end{cases} \tag{2.27}$$

Where E_p is the Young's modulus of proppants, $\boldsymbol{w}$ is the fracture opening displacement, D_i is the initial fracture aperture. Eq. (2.27) shows that a proppant is only effective when fracture aperture is being decreased.

2.5 Introduction to XFEM

To model the discontinuity field, enrich based FEM are applied a lot nowadays. The enrichment is realized through the basic mathematical foundation of the partition of unity finite element method (PUFEM) was discussed by Melenk and Babuška (1996). The global solution of PUFEM has been the theoretical basis of the extended finite element.

XFEM has a lot of advantages. One new feature of XFEM is that only local parts of the domain are enriched and this localization is achieved by enriching a subset of nodes (Moës et al. 1999). And cost of computation is reduced much more because of localized enrichment. Moreover, many more complicated physical phenomenon are also easier to simulate by means of XFEM. Because fractures are independent representation of the entire crack from the mesh, no re-meshing is required when fracture propagation is involved. And it is easy to extend to heterogeneous or even nonlinear mechanical property problems.

In **Fig. 2.7**, the different types of elements (standard, blending, enriched) and nodes (standard, Heaviside enriched, Tip function enriched) are shown. In the standard and enriched element, partition of unity is satisfied. The blending element is no longer a partition of unity. Nevertheless, it has little direct effect on the approximation because blending element does not include singularity. The appearance of blending elements especially for those near fracture tip could decrease the convergence rate of XFEM (Fries and Belytschko, 2010).

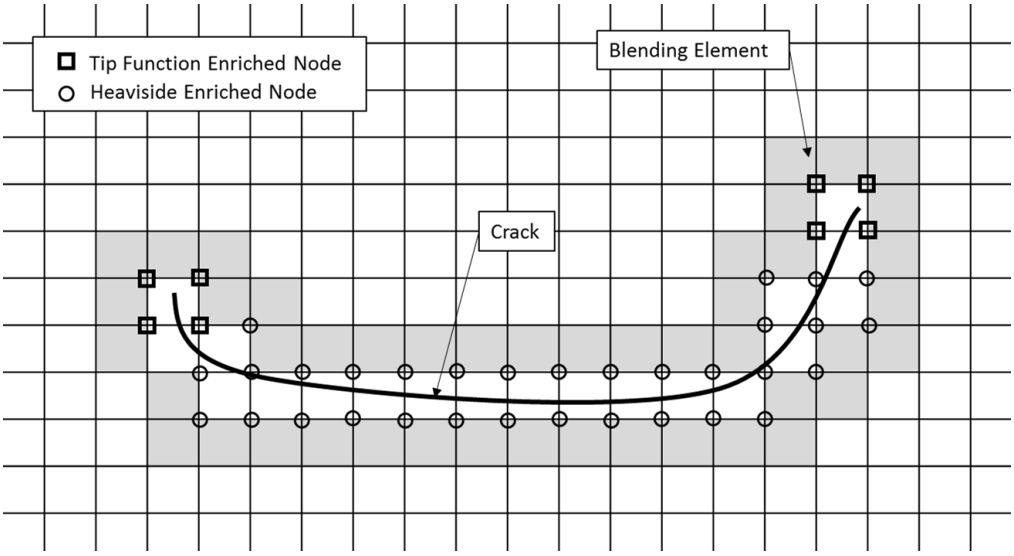

Figure 2.7 different types of elements and nodes

For X-FEM, Moës et al. (1999) proposed an equation that can model crack surfaces and tips by step functions and asymptotic near-tip fields. The finite element approximation for a single crack in a two-dimensional body can be written as:

$$\boldsymbol{u^h}(\boldsymbol{x}) = \sum_{i\in I} N_i(x)\boldsymbol{u_i} + \sum_{i\in L} N_i(x)H\big(\xi(x)\big)\boldsymbol{a}_i + \sum_{i\in K_1} N_i(x)\Big(\sum_{l=1}^{4} F_l(x)\boldsymbol{b}_{i,1}^{l}\Big) + \sum_{i\in K_2} N_i(x)\Big(\sum_{l=1}^{4} F_l(x)\boldsymbol{b}_{i,2}^{l}\Big) \qquad (2.28)$$

Where I is the set of all nodes in the mesh; $\boldsymbol{u}_i$ is the classical degree of freedom at node i; N_i is the shape function associated with node i. $L \subset I$ is the subset of nodes that are enriched for the crack discontinuity and $\boldsymbol{a}_i$ are corresponding additional degrees of freedom; the nodes in L are such that their support (elements that are connected by a node) intersects the crack but do not contain any of its crack tips; and $K_1 \subset I$ and $K_2 \subset I$ are the subset of nodes that are enriched for the first and second crack tip, respectively. The corresponding additional degrees of freedom are $\boldsymbol{b}_{i,1}^{l}$ and $\boldsymbol{b}_{i,2}^{l}, l = 1, \dots, 4$,for the first and second crack tip, respectively.

Illustration of signed distance function is shown in **Fig. 2.8**, its definition is given as the following:

$$\xi(\boldsymbol{x}) = min\,\|\boldsymbol{x} - \boldsymbol{x}_{\Gamma}\|sign\big(\boldsymbol{n}\cdot(\boldsymbol{x} - \boldsymbol{x}_{\Gamma})\big) \tag{2.29}$$

Where $\boldsymbol{x}_{\Gamma}$ is projection of $\boldsymbol{x}$ onto an arbitrary surface. $\boldsymbol{n}$ is the unit out normal vector of the surface.

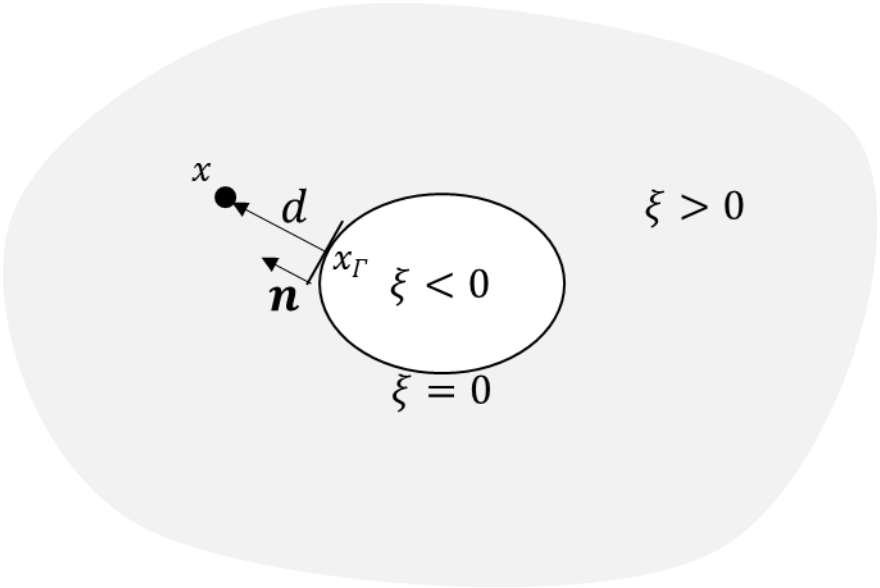

Figure 2.8 Schematic of signed distance function

Heaviside Function is defined as:

$$H(\xi) = \begin{cases} 1 & \forall\xi > 0 \\ -1 & \forall\xi < 0 \end{cases} \tag{2.30}$$

The near tip enrichment functions have already been defined in terms of local crack tip coordinate system(r, θ). Note that only the first function in Eq. (2.31) is discontinuous across the surface $(\pm\pi)$ whereas the other three functions are continuous.

$$F_l(r,\theta) = \left\{\sqrt{r}\,sin\frac{\theta}{2}, \sqrt{r}\,cos\frac{\theta}{2}, \sqrt{r}\,sin\,\theta\,sin\frac{\theta}{2}, \sqrt{r}\,sin\,\theta\,cos\frac{\theta}{2}\right\} \tag{2.31}$$

To model discontinuity, virtual nodes are imposed onto the standard nodes and combined with classical finite element method to approximate displacement field. In order to clarify how this method works, we will illustrate it through a one dimensional problem which consists of four nodes and three elements with a strong discontinuity. There is a discontinuity between node 2 and 3. In **Fig. 2.10** and **Fig. 2.11**, the approximation function at the left and right discontinuity point is totally different. And if the approximation function is added to the standard finite element shape function, discontinuous displacement field will be obtained. We also notice that the displacement at each node in **Fig. 2.10** is the following:

$$\boldsymbol{u^h} = \boldsymbol{u_i} + H(\xi_i)\boldsymbol{a_i} \tag{2.32}$$

At each node, the displacement is not equal to $\boldsymbol{u_i}$, which does not satisfy the interpolation. However, in **Fig. 2.11**, because of the shifted function, $\boldsymbol{u}^h = \boldsymbol{u_i}$, shift function will not cause any blending any elements either.

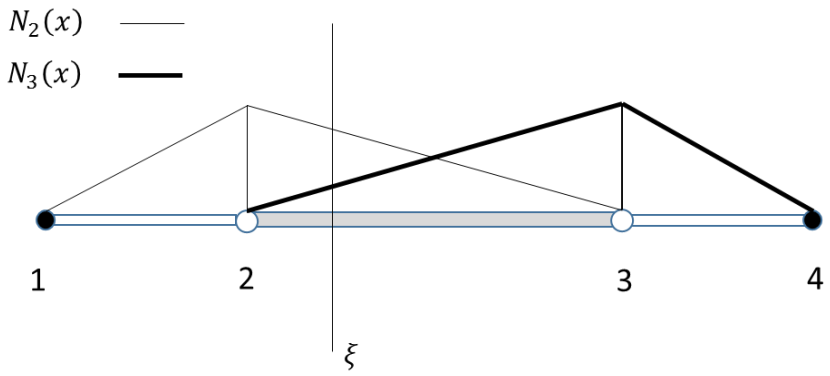

Figure 2.9 Standard shape function for node 2 and 3

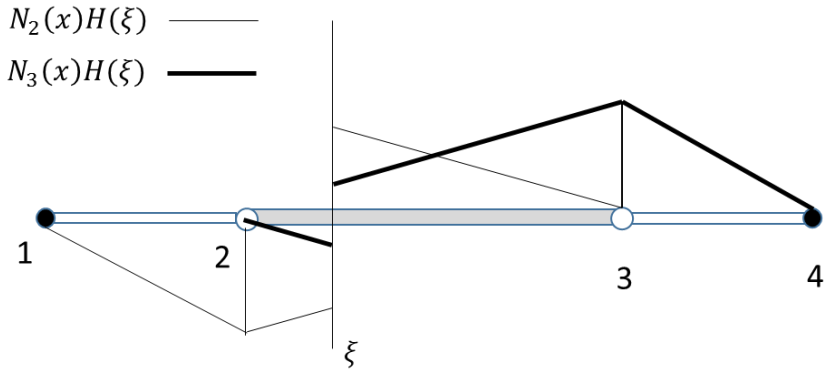

Figure 2.10 Enriched shape function for node 2 and 3

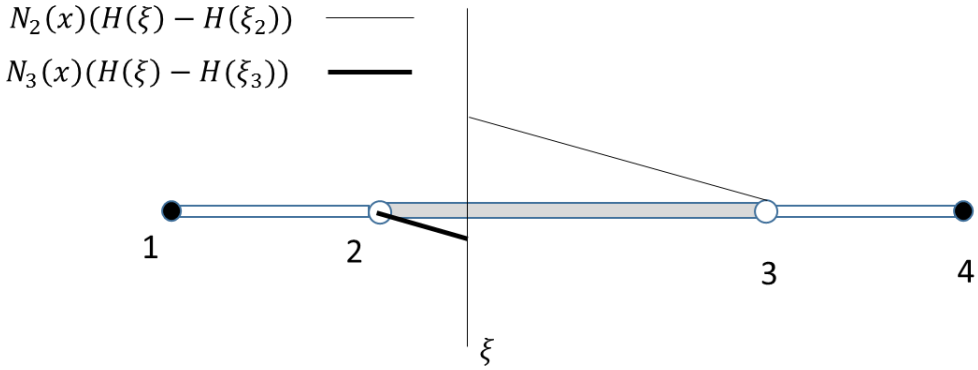

Figure 2.11 Shifted enriched function for node 2 and 3

2.6 Weak Form and coupled XFEM with Dual Porosity Discretization

2.6.1 Weak Form

The weak form of equilibrium equation (neglecting body force) is given by (Chen 2013, Khoei 2014, Mohammadi 2008) and we extend it to include dual porosity and proppant models.

The space of the admissible solution for displacement $\boldsymbol{u}$ is defined as:

$$\mathcal{U} = \{\mathbf{v} \in \mathcal{V}, \mathbf{v} = \bar{\boldsymbol{u}} \text{ on } \Gamma_u, \mathbf{v} \text{ discontinous on } \Gamma_c\} \tag{2.33}$$

Where the space $\mathcal{V}$ is related to the regularity of the solution in which **v** is discontinuous over the fracture. The test function is defined similarly as:

$$\mathcal{U}_0 = \{\mathbf{v} \in \mathcal{V}, \mathbf{v} = 0 \text{ on } \Gamma_u, \mathbf{v} \text{ discontinous on } \Gamma_c\} \tag{2.34}$$

The weak form is to find $\boldsymbol{u} \in \mathcal{U}$ such that the solution satisfies equilibrium equation. The weak form is derived by Galerkin method and given by:

$$\int_\Omega \delta\boldsymbol{\varepsilon}: D_{mf}: \boldsymbol{\varepsilon} d\Omega = \int_\Omega \delta\boldsymbol{\varepsilon}: \alpha_m^* p_m \boldsymbol{I} d\Omega + \int_\Omega \delta\boldsymbol{\varepsilon}: \alpha_f^* p_f \boldsymbol{I} d\Omega + \int_{\Gamma_t} \delta\boldsymbol{u} \cdot \boldsymbol{t} d\Gamma_t$$
$$+ \int_{\Gamma_c^+} (\delta\boldsymbol{u}^+ - \delta\boldsymbol{u}^-) \cdot \bar{\boldsymbol{p}}\, d\Gamma_c + \int_{\Gamma_c^+} (\delta\boldsymbol{u}^+ - \delta\boldsymbol{u}^-) \cdot \boldsymbol{p}_p d\Gamma_c \tag{2.35}$$

Where $\delta\boldsymbol{u}$ and $\delta\boldsymbol{\varepsilon}$ are virtual displacement and strain respectively. We assume that matrix pore pressure p_m and natural fracture pressure p_f that is effective only on normal direction. Shear force is neglected on matrix caused by fluid flow. On the outer boundary Γ_t, which is the boundary of the reservoir, force $\boldsymbol{t}$ is applied. On the inner boundary or discontinuity boundary Γ_c^+ or Γ_c^-, $\boldsymbol{u}^+$ and $\boldsymbol{u}^-$ are displacements on the fracture upper and lower faces separately. Besides fluid pressure $\bar{\boldsymbol{p}}$, proppant force $\boldsymbol{p}_p$is also considered and only active where fracture has a tendency to close.

We can write out equation calculating crack opening displacement $\boldsymbol{w}$:

$$\boldsymbol{w} = \boldsymbol{n_c} \cdot (\boldsymbol{u}^+ - \boldsymbol{u}^-)\boldsymbol{n_c} \tag{2.36}$$

Eq. (2.35) can be simplified by substitution of Eq. (2.36). Then the equation will be like:

$$\int_\Omega \delta\boldsymbol{\varepsilon}: D_{mf}: \boldsymbol{\varepsilon} d\Omega = \int_\Omega \delta\boldsymbol{\varepsilon}: \alpha_m^* p_m \boldsymbol{I} d\Omega + \int_\Omega \delta\boldsymbol{\varepsilon}: \alpha_m^* p_f \boldsymbol{I} d\Omega + \int_{\Gamma_t} \delta\boldsymbol{u} \cdot \boldsymbol{t} d\Gamma_t +$$

$$\int_{\Gamma_c^+} \delta\boldsymbol{w} \cdot (\overline{\boldsymbol{p}} + \boldsymbol{p}_p)\, d\Gamma_c \tag{2.37}$$

2.6.2 Discretization

Using the standard Galerkin procedure to discretize the system results a system of linear equilibrium equations.

$$\boldsymbol{K}\boldsymbol{u}^h = \mathbf{f} \tag{2.38}$$

Where $\boldsymbol{K}$ is global stiffness matrix, $\boldsymbol{u}^h$ is the degree of freedoms for both standard nodes and enriched nodes and $\mathbf{f}$ is the force vector. We usually assemble stiffness matrix and force vector element by element. In each element, the local stiffness matrix $\boldsymbol{K}_e$ and $\mathbf{f}_e$ has the following pattern:

$$\boldsymbol{K}_e = \begin{pmatrix} K_{ij}^{\mathrm{uu}} & K_{ij}^{\mathrm{ua}} & K_{ij}^{\mathrm{ub}} \\ K_{ij}^{\mathrm{au}} & K_{ij}^{\mathrm{aa}} & K_{ij}^{\mathrm{ab}} \\ K_{ij}^{\mathrm{bu}} & K_{ij}^{\mathrm{ba}} & K_{ij}^{\mathrm{bb}} \end{pmatrix} \tag{2.39}$$

and

$$\mathbf{f}_e = (\mathbf{f}_{\mathrm{i}}^{\mathrm{u}}, \mathbf{f}_{\mathrm{i}}^{\mathrm{a}}, \mathbf{f}_{\mathrm{i}}^{\mathrm{b}_\alpha}) \tag{2.40}$$

Where i, j is the node number which ranges from 1 to 4 in each element. α varies from 1 to 4. $\mathrm{u}, \mathrm{a}, \mathrm{b}_\alpha$ represent standard, Heaviside, Tip function enriched node respectively. With

the linear fracture, each node in the element with a fracture tip in it is enriched by four asymptotic functions Eq. (2.31).

In each element, element stiffness matrix $\boldsymbol{K}_{ij}^{rs}$ and force vectors $\mathbf{f}_i^{\mathrm{u}}$, $\mathbf{f}_i^{\mathrm{a}}$, $\mathbf{f}_i^{\mathrm{b}\alpha}$ are defines as:

$$\boldsymbol{K}_{ij}^{rs} = \int_{\Omega_e} (\mathbf{B}_i^{\mathrm{r}})^{\mathrm{T}} D_{mf} \mathbf{B}_j^{\mathrm{s}} d\Omega_e \ (\mathrm{r,s} = \mathrm{u,a,b}_\alpha)(i,j = 1..4) \tag{2.41}$$

$$\mathbf{f}_i^{\mathrm{u}} = \int_{\Gamma_t} N_i \mathbf{t} \mathrm{d}\Gamma_t + \int_{\Omega_e} (\mathbf{B}_i^{\mathbf{u}})^{\mathrm{T}} (\alpha_f^* p_f + \alpha_m^* p_m) d\Omega_e \tag{2.42}$$

$$\mathbf{f}_i^{\mathrm{a}} = \int_{\Gamma_t} N_i H \mathbf{t} \mathrm{d}\Gamma_t + \int_{\Gamma_c} 2N_i (\overline{\boldsymbol{p}} + \boldsymbol{p}_p) d\Gamma_c + \int_{\Omega_e} (\mathbf{B}_i^{\mathrm{a}})^{\mathrm{T}} (\alpha_f^* p_f + \alpha_m^* p_m) d\Omega_e \tag{2.43}$$

$$\mathbf{f}_i^{\mathrm{b}\alpha} = \int_{\Gamma_t} N_i F_\alpha \mathbf{t} \mathrm{d}\Gamma_t + \int_{\Gamma_c} 2N_i F_1(r, \theta = \pi)\big(\overline{\boldsymbol{p}} + \boldsymbol{p}_p\big) d\Gamma_c +$$

$$\int_{\Omega_e} (\mathbf{B}_i^{\alpha})^{\mathrm{T}} (\alpha_f^* p_f + \alpha_m^* p_m)\, d\Omega_e \tag{2.44}$$

$$\mathbf{B}_i^{\mathrm{u}} = \begin{bmatrix} N_{i,x} & 0 \\ 0 & N_{i,y} \\ N_{i,y} & N_{i,x} \end{bmatrix} \tag{2.45}$$

$$\mathbf{B}_i^{\mathrm{a}} = \begin{bmatrix} N_i[H(\xi) - H(\xi_i)]_{,x} & 0 \\ 0 & N_i[H(\xi) - H(\xi_i)]_{,y} \\ N_i[H(\xi) - H(\xi_i)]_{,y} & N_i[H(\xi) - H(\xi_i)]_{,x} \end{bmatrix} \tag{2.46}$$

$$\mathbf{B}_i^{\mathrm{b}\alpha} = \begin{bmatrix} [N_i(F_\alpha - F_{\alpha i})]_{,x} & 0 \\ 0 & [N_i(F_\alpha - F_{\alpha i})]_{,y} \\ [N_i(F_\alpha - F_{\alpha i})]_{,y} & [N_i(F_\alpha - F_{\alpha i})]_{,x} \end{bmatrix} (\alpha = 1,2,3,4) \tag{2.47}$$

Where $\mathbf{B}_i^{\mathrm{u}}$ is the derivative of standard node shape function. $\mathbf{B}_i^{\mathrm{a}}$ is the derivative of Heaviside enrichment shape function. $\mathbf{B}_i^{\mathrm{b}\alpha}$ is the derivative of tip enrichment shape function.

2.6.3 Numerical Integration

The Gauss quadrature rule is successfully being used for the numerical integration in finite element analysis. For polynomial integrand, the Gauss quadrature is proved to be correct. However, in the XFEM, we introduce the linear discontinuous function which is Heaviside function and nonlinear, singular and discontinuous function which is tip enrichment functions. Poor accuracy can be achieved without any special treatment. Next, we will apply two different numerical integration schemes especially for Heaviside enrichment and tip enrichment shape functions respectively.

For the element cut by a crack, Dolbow (1999) proposed two methods to overcome this integration difficulty. In the first method, element that is cut by fracture is subdivided into many sub triangles. Ordinary Gauss quadrature rule is performed on each sub triangle where the integrand is continuous polynomial. The second one is to subdivide element into sub-quads. Compared to the second method, the first one should be more efficient and accurate. The first method is illustrated in the **Fig. 2.12.**

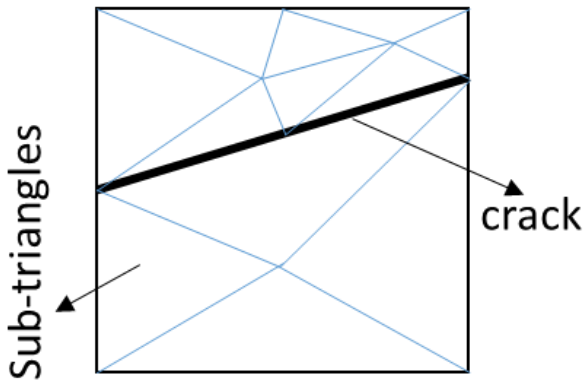

Figure 2.12 Partition of the element with sub triangles

For the element containing crack tips, the derivative of the tip enrichment shape functions will introduce singularity term as well as discontinuity. Thus a special quadrature rule is highly recommended for singular integrand. Owing to high gradients near the singularity, a concentration of integration points in the vicinity of the singularity improves the results significantly. The numerical integration procedure is listed below:

1. Element is subdivided into sub-triangles.
2. Tensor product-type Gaussian quadrature rule is performed on each sub-triangular elements
3. Sum up the integration values from each sub elements

The idea of Tensor product-type Gaussian quadrature rule is to transform the standard triangular element T_{st} to the standard quadrilateral element R_{st} and then apply Gauss quadrature for R_{st}. The advantage of this method is that the location of the Gauss points is concentrated on a relatively small region near one vertex. The following picture shows the procedure of the numerical integration for elements containing tips.

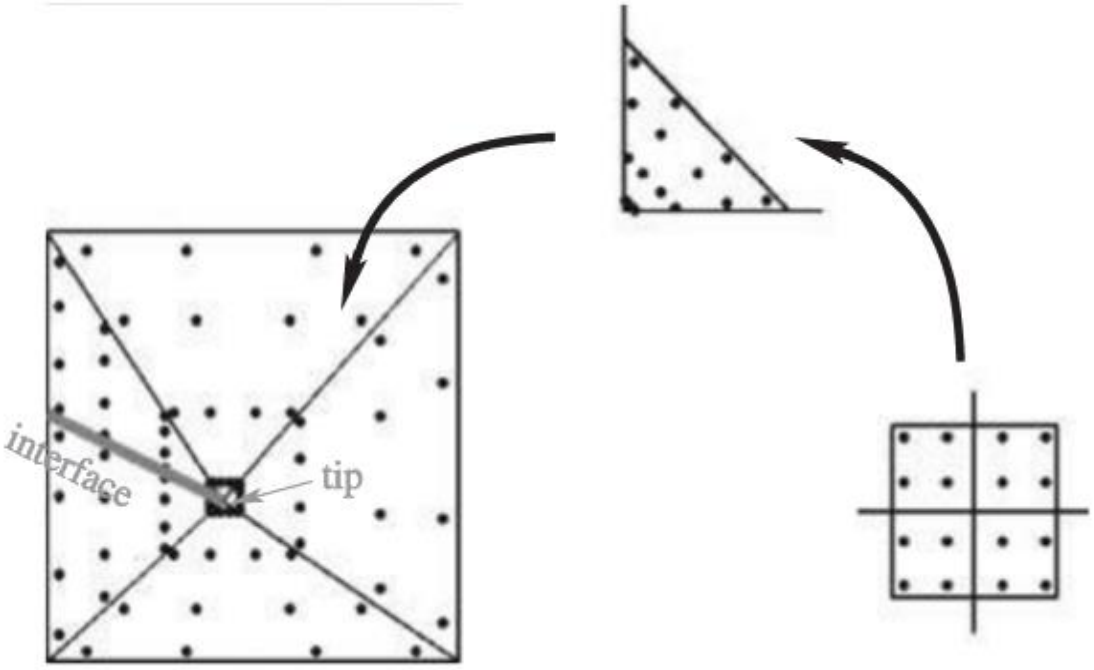

Figure 2.13 Integration points in an element containing a singularity (Fries and Belytschko, 2010)

CHAPTER 3

FLUID FLOW MODELS

In this session, we shall derive mass balance equations for two phase black oil in deformable porous media. The development of the system of the governing equations is based on the following general assumptions:

1. Rock behaves as isothermal linear poroelasticity,
2. Geomechanics process is under quasi-static equilibrium.
3. The deformation of the porous media is infinitesimal.

We will introduce the flow modes, EDFM and dual porosity model for fluid flow. In the following poromechanics equations, the sign convention is adopted positive for tension and negative for compression.

3.1 Governing Equation for single fluid flow

The primary variables in the resulting system of governing equations are the fluid pressure (p) and displacement (u). First we derive the single phase flow equation in deformable porous media.

Mass Conservation of the solid phase:

$$\frac{\partial \rho_s(1-\phi)}{\partial t} + \nabla \cdot (\rho_s(1-\phi)\boldsymbol{V}^s) = 0 \tag{3.1}$$

Mass Conservation of the fluid phase:

$$\frac{\partial \rho_f \phi}{\partial t} + \nabla \cdot \left(\rho_f \phi \boldsymbol{V}^f\right) = 0 \tag{3.2}$$

Where ρ_α is the phase density, ϕ is the porosity, $\boldsymbol{V}^\alpha$is the phase velocity. $\alpha =$ solid phase (s), fluid phase (f) .

$$\frac{\partial \rho_f \phi}{\partial t} + \nabla \cdot \left(\rho_f \phi \boldsymbol{V}^s\right) + \nabla \cdot \left(\rho_f \phi (\boldsymbol{V}^f - \boldsymbol{V}^s)\right) = 0 \tag{3.3}$$

And the third term in Eq. (3.3) on the left can be replaced by Darcy's velocity

$$\frac{\partial \rho_f \phi}{\partial t} + \rho_f \phi \nabla \cdot (\boldsymbol{V}^s) + \boldsymbol{V}^s \cdot \nabla(\rho_f \phi) + \nabla \cdot \left(\rho_f \boldsymbol{V}^D\right) = 0 \tag{3.4}$$

Now, we define material derivative as the following:

$$\frac{D(\quad)}{Dt} = \frac{\partial(\quad)}{\partial t} + \boldsymbol{V^s} \cdot \nabla(\quad) \tag{3.5}$$

Then, we can write the Eq. (3.4) in terms of using material derivative.

$$\frac{D(\rho_f \phi)}{Dt} + \rho_f \phi \nabla \cdot (\boldsymbol{V}^s) = -\nabla \cdot \left(\rho_f \boldsymbol{V}^D\right) \tag{3.6}$$

Eq. (3.1) follows the same procedure and the result is:

$$\nabla \cdot \boldsymbol{V}^s = -\frac{1}{(1-\phi)\rho_s} \frac{D(1-\phi)\rho_s}{Dt} \tag{3.7}$$

If we assume a constant solid mass ($D(\rho_s V_s) = 0$), and using $\phi = \frac{V_p}{V_b} = 1 - \frac{V_s}{V_b}$, ($V_b$, V_p and V_s are the bulk, pore and solid volume respectively), we can further simplify the Eq. (3.7) into:

$$\nabla \cdot \boldsymbol{V}^s = \frac{1}{V_b} \frac{DV_b}{Dt} \tag{3.8}$$

From the definition of volume strain, we know that:

$$\epsilon_v = \frac{DV_b}{V_b} \tag{3.9}$$

Thus, Eq. (3.9) substitutes into Eq. (3.8) and we get:

$$\nabla \cdot \boldsymbol{V}^s = \frac{D\epsilon_v}{Dt} \tag{3.10}$$

Therefore, divergence of solid phase velocity only reflects rate of bulk volume changes. Next we substitute Eq. (3.10) above into the fluid flow Eq. (3.6) and we get:

$$\frac{D(\rho_f \phi)}{Dt} + \rho_f \phi \frac{D\epsilon_v}{Dt} = -\nabla \cdot \left(\rho_f \boldsymbol{V}^D\right) \tag{3.11}$$

We add and subtract the term $\epsilon_v \frac{D\rho_f \phi}{Dt}$ into Eq. (3.11):

$$\frac{D(\rho_f \phi)}{Dt} + \rho_f \phi \frac{D\epsilon_v}{Dt} + \epsilon_v \frac{D\rho_f \phi}{Dt} - \epsilon_v \frac{D\rho_f \phi}{Dt} = -\nabla \cdot \left(\rho_f \boldsymbol{V}^D\right) \tag{3.12}$$

Then the second and third term in the left hand side can be combined into one:

$$\frac{D(\rho_f \phi)}{Dt} + \frac{D\rho_f \phi \epsilon_v}{Dt} - \epsilon_v \frac{D\rho_f \phi}{Dt} = -\nabla \cdot \left(\rho_f \boldsymbol{V}^D\right) \tag{3.13}$$

Now we recall the assumption that the deformation is infinitesimal, which means ϵ_v is very small. Therefore, the third term in the left hand side $\epsilon_v \frac{D\rho_f \phi}{Dt}$ is much smaller compared to the first term and can be neglected. Thus the Eq. (3.13) is written as the following:

$$\frac{D\rho_f \phi(1+\epsilon_v)}{Dt} = -\nabla \cdot \left(\rho_f \boldsymbol{V}^D\right) \tag{3.14}$$

We usually define $\phi^* = \phi(1 + \epsilon_v)$ as the fluid traction or the Lagrangian porosity. Because of the infinitesimal deformation, the Lagrangian description and Eulerian description is the same as each other. Therefore, $\partial(\,)/\partial t \approx D(\,)/Dt$. Finally, the governing equation considering geomechanics effect for fluid flow (no source/sink term) is written as the following:

$$\frac{\partial \rho_f \phi^*}{\partial t} = -\nabla \cdot \left(\rho_f \boldsymbol{V}^D\right) \tag{3.15}$$

In the section 3.5, we will extend the equation of single phase flow to one of two phase flow.

3.2 EDFM Model

Lee et al. (2001), Li and Lee (2008), Hajibeygi et al. (2011) and Moinfar et al. (2012) developed and improved the embedded discrete fracture model. EDFM applies the concept of wellbore index (WI) to derive a transport index between fracture and matrix cells. Moinfar et al. (2013) show that EDFM provides adequate accuracy for multiphase compositional simulation.

Because the fractures and the matrix are modeled on different computational domains, there is no fluid communication between them in the mass balance equations. Consequently, we define non-neighboring connections (NNC) for EDFM. That is, each gridblock in the numerical model can communicate with any other gridblock through a non-neighboring connection.

The embedded fracture3s are discretized vertically and horizontally by the cell boundaries of gridblocks that are intersected by a fracture. Connection transmissibility is then introduced to account for the flux interaction between the fracture and the matrix. Li and Lee 2008 assume that the pressure around fracture is linearly distributed, and with this approximation the average normal distance from the fracture in the gridblock is

$$\langle d \rangle = \frac{\int \boldsymbol{n} \cdot x dS}{S} \tag{3.16}$$

where $\boldsymbol{n}$ is the unit normal vector; x is the distance from the fracture; dS and S are the areal element and area of the gridblock, respectively. Subsequently, the transmissibility is

$$T = \frac{kA}{\langle d \rangle} \tag{3.17}$$

where A is the fracture surface area in the gridblock and k is the harmonic average of the permeability of the hydraulic fracture and the matrix. For fractures that do not fully

penetrate a gridblock, it is assumed that T is linearly proportional to the fracture length inside the gridblock; therefore, the transfer term between a matrix cell and a segment of a fracture embedded in that cell is

$$q_{mf} = T(\psi_m - \psi_f) \tag{3.18}$$

where q_{mf} is the volumetric rate between the matrix gridblock and the fracture segment, T is the transmissibility between them, ψ_m and ψ_f are matrix and fracture gridblock potential, respectively.

For a NNC between intersecting fracture cells, we use the same approach presented by Karimi-Fard et al. (2004), wherein the transmissibility is

$$\mathrm{T}_{ff} = \frac{T_1 T_2}{T_1 + T_2} \tag{3.19}$$

$$T_1 = \frac{k_{f1}\omega_{f1}L_{int}}{d_{f1}} \qquad T_2 = \frac{k_{f2}\omega_{f2}L_{int}}{d_{f2}} \tag{3.20}$$

where L_{int} is the length of the intersection line bounded in a gridblock, ω_f is fracture aperture and k_f is fracture permeability. Likewise, d_f is the average of normal distances from the center of the fracture subsegments (located in each side of the intersection line) to the intersection line.

Such a NNC is required for any pair of intersecting fractures. Thus, if more than two fractures intersect in a gridblock, a NNC is defined between each pair of intersecting fracture control volumes. Also, if two fractures penetrating a gridblock do not intersect with each other within the gridblock, no NNC is needed.

For a NNC between two cells of an individual fracture, k is equal to the fracture permeability and d is the distance between the centers of two fracture segments. Parameter A is the fracture aperture times the length of this intersection line.

Before fluid-flow simulation, a list of NNC pairs, the arrangement of fracture cells, the arrangement of fracture cells, the transmissibility of NNCs, and the transmissibility between fracture cells should be computed on the basis of the grid structure and fracture planes. A preprocessing code is developed to provide the required data for flow simulations.

While EDFM facilitates the modeling of irregular fracture geometry, it is not very appropriate for unconventional reservoir modeling for the reason that it assumes a linear pressure variation in the normal direction to each fracture. The extreme contrast in conductivity between fractures and the ultra-tight matrix results in steep potential gradients that are difficult to capture.

3.3 Dual Continuum Model

Dual-continuum models, widely used in the industry, are the conventional method for simulating NFRs. Warren and Root (1963) introduced the dual porosity model to the petroleum literature. The dual porosity model, which is also known as a sugar cube model, was first used for modeling single-phase flow in NFRs. In this model, rectilinear prisms of rock matrix are separated by an orthorhombic continuum of fractures. Dual porosity simulation involves discretization of the reservoir into two domains, matrix and fracture. Hence, every point in the reservoir contains fracture and matrix pressures and saturations. A dual porosity model presumes that the flow occurs from the matrix to the fractures, and then to the production wells. The rock matrix is where the majority of oil is stored. In the dual porosity model, matrix and fracture domains are linked to each other through an exchange term that connects each fracture cell to its corresponding matrix cell in a

gridblock. The matrix-fracture exchange rate is controlled by a shape factor. Also, the matrix blocks in the dual porosity approach are assumed to be isotropic and homogeneous. **Fig. 3.1** shows an idealized sugar cube representation of a fractured reservoir, wherein highly interconnected orthogonal fractures are fed by numerous matrix blocks.

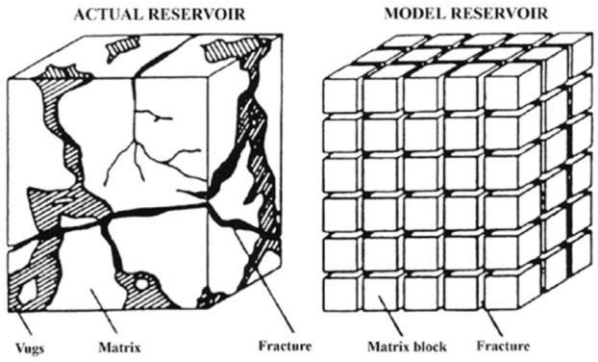

Figure 3.1: An idealized sugar cube representation of a fractured reservoir (Warren and Root 1963).

Considering single-phase fluid flow, the mass conservation equations for the fracture and matrix domains in the dual porosity approach can be expressed for the fracture domain, as

$$\frac{k_{fx}}{\mu}\frac{\partial^2 P_f}{\partial x^2}+\frac{k_{fy}}{\mu}\frac{\partial^2 P_f}{\partial y^2}+\frac{k_{fz}}{\mu}\frac{\partial^2 P_f}{\partial z^2}-q_{mf}=\phi_f C_f\frac{\partial P_f}{\partial t} \tag{3.21}$$

and for the matrix domain, as

$$\phi_m C_m\frac{\partial P_m}{\partial t}=q_{mf} \tag{3.22}$$

The matrix-fracture transfer is represented by the pseudo-steady state relation

$$q_{mf}=\frac{\sigma k_m}{\mu}\left(P_m-P_f\right) \tag{3.23}$$

where k is permeability, P is pressure, μ is fluid viscosity, C is total compressibility, ϕ is porosity, σ is shape factor, and q_{mf} is matrix-fracture flow rate per unit bulk volume. The subscripts m and f refer to the properties in the matrix and fracture domains. The shape

factor, which has the dimension of reciprocal area, reflects the geometry of matrix blocks and controls the interporosity flow between matrix and fracture domains.

3.3.1 Shape Factor

The matrix-fracture exchange is a critical component of any model used for the simulation of NFRs. In the Warren and Root approach, the matrix-fracture fluid transfer is assumed to take place under pseudo-steady state conditions. The matrix-fracture transfer function is proportional to a geometrical shape factor σ, and the driving force is the pressure difference between a matrix block and its surrounding fracture. Determination of shape factor is not a simple task because of the potential for complex interaction between fractures and matrix rock of various shapes.

Originally, Warren and Root (1963) defined the shape factor as a parameter that depends on the geometry of matrix blocks, as

$$\sigma = \frac{4n(n+2)}{L^2}, \tag{3.24}$$

where n is the number of normal sets of fractures $(n = 1, 2, 3)$ and the characteristic length of matrix blocks

$$\begin{aligned} L &= a, && n = 1 \\ L &= \frac{2ab}{a+b}, && n = 2 \\ L &= \frac{3abc}{ab+ac+bc}, && n = 3 \end{aligned} \tag{3.25}$$

where a, b, and c are the lengths of the blocks faces.

Kazemi et al. (1976) used a finite-difference formulation for the flow between matrix and fractures and showed that for a three-dimensional case

$$\sigma = 4\left(\frac{1}{L_x^2} + \frac{1}{L_y^2} + \frac{1}{L_z^2}\right) \tag{3.26}$$

where L_x, L_y, and L_z are the distances between fractures in the x, y, and z directions, respectively.

These shape factors assume that the pseudo-steady state assumption is valid. Lim and Aziz (1995) considered the physics of pressure diffusion from the matrix to the fracture and presented a new shape factor as follows

$$\sigma = \pi^2\left(\frac{1}{L_x^2} + \frac{1}{L_y^2} + \frac{1}{L_z^2}\right) \tag{3.27}$$

They performed simulations to investigate the accuracy of various shape factors using fine-grid simulations. The results showed that their shape factor in Eq. (3.27) matches with the results of fine-grid single porosity better, indicating that the pseudo-steady state assumption is not a suitable one and the pressure gradients in the matrix should be taken into account for the calculation of shape factors. They also showed that the dual porosity simulation using the Warren and Root's shape factor overestimates the recovery, while the simulation using the Kazemi's shape factor underestimates the recovery.

3.4 Geomechanics Effect on porosity and permeability

3.4.1 Geomechanics effect on porosity and permeability of dual continuum

We assume natural fractures consists of continuum alike matrix which has the concept porosity. Porosity is a function of volume strain and fluid pressure. Thus the same type of equation for porosity update can apply to both. Gai et al. (2003) provides the relationship between porosity and fluid pressure and volumetric strain under infinitesimal deformation.

$$\phi^* = \phi^0 + \alpha\epsilon_v + \frac{1}{M}p \tag{3.28}$$

Where ϕ^0 is the initial porosity in each continuum, α and $M^{-1}$are Biot's coefficient and Biot's poroelastic parameter for matrix or natural fracture continuum. p is the pressure of matrix.

In unconventional reservoir, the permeability of matrix is considerable small (10^{-17}~10^{-20} m^2). Thus the change of matrix permeability has a little effect on flow compared to that of natural and hydraulic fractures. We assume matrix permeability is constant.

The permeability in natural fractures are mainly affected by the aperture. According to the cubic law, the permeability of the cracked system (Izadi, 2011) may be expressed as:

$$\frac{k}{k_0} = \left(1 + \frac{\Delta b}{b_0}\right)^3 \tag{3.29}$$

Where Δb is the aperture change in natural fracture which is a function of strain. b_0 is the initial aperture of natural fracture.

That aperture change is a function of strain has been supported by previous research (Liu, 2010). We calculate the average fracture aperture change Δb in x and y directions for each grid block. In **Fig. 3.2**, S is the spacing of natural fracture. b is the natural fracture aperture.

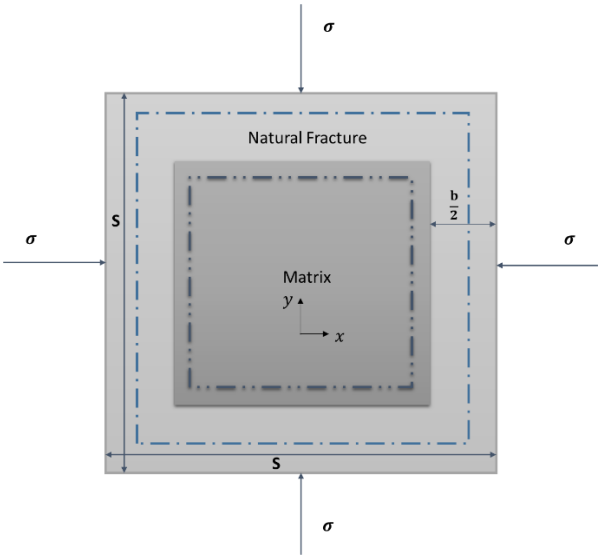

Figure 3.2. Schematic diagram of fracture aperture change due to strain. Solid line boundary and Dashed line boundary are the configuration before and after deformation.

We can derive the relationship between average aperture and strain changes due to the external force. From the definition of volume strain, we write out volumetric strain of total and matrix individually.

$$\epsilon = \frac{\Delta x}{S} + \frac{\Delta y}{S} \tag{3.30}$$

$$\epsilon_m = \frac{\Delta x - \Delta b}{S} + \frac{\Delta y - \Delta b}{S} \tag{3.31}$$

Where Δx and Δy are the length changes in x and y directions.

Plug Eq. (3.30) and (3.31) into $\varepsilon = \varepsilon_m + \varepsilon_f$, we get :

$$\Delta b = \frac{S\epsilon_f}{2} \tag{3.32}$$

For the scenario that each dual porosity grid block is cut by hydraulic fracture, there is a discontinuity of strain across the hydraulic fracture. We calculate strains for two regions that is separated by hydraulic fracture in each grid block and take the average value ϵ_f from each part.

3.4.2 Geomechanics Effect on hydraulic fracture permeability

We treat hydraulic fracture as void space, that is, porosity is unity and consider permeability is the function of the fracture aperture. According to the Poiseuille law, the fracture permeability is proportional to the fracture aperture square (Moinfar et al., 2013):

$$k_f = k_f^0 \left(\frac{\omega_f}{\omega_f^0}\right)^2 \tag{3.33}$$

3.5 Discretization

In the flow simulation, we use fully implicit, first order backward Euler scheme in time and finite volume method to discretize flow equations. In the following equations, subscript $\alpha =$ gas or water. Subscripts m, f, F represent matrix, natural fracture and hydraulic fracture individually. Superscript n means the time step.

For matrix i, we only consider the fluid flow is between matrix continuum and surrounding natural fracture continuum. The discretized form is the following:

$$\left(V_i S_{\alpha,i} \rho_{\alpha,i} \phi^*_{m,i}\right)^{n+1} - \left(V_i S_{\alpha,i} \rho_{\alpha,i} \phi^*_{m,i}\right)^n - \Delta t \left(T_{\alpha,mf,ii} \frac{k_{r\alpha}}{\mu_\alpha} \rho_\alpha \Delta\Phi_{\alpha,mf,ii}\right)^{n+1} = 0 \tag{3.34}$$

Where V_i is the volume of the grid block i, $\phi^*_{m,i}$ is the fluid fraction of matrix i, $T_{\alpha,mf,ii}$ is the transmissibility between matrix i and natural fractures i. Δt is the time step, $\Delta\Phi_{\alpha,mf,i}$ is the potential difference between matrix i and the natural fracture i.

For natural fracture continuum i, besides the flow between matrix and itself, it also has flow connection with hydraulic fractures that cut natural fractures.

$$\left(V_i S_{\alpha,i} \rho_{\alpha,i} \phi^*_{f,i}\right)^{n+1} - \left(V_i S_{\alpha,i} \rho_{\alpha,i} \phi^*_{f,i}\right)^n$$

$$+\Delta t\left(T_{\alpha,mf,ii}\frac{k_{r\alpha}}{\mu_\alpha}\rho_\alpha\Delta\Phi_{\alpha,mf,ii}\right)^{n+1}-\sum_{j=1}^{n_{faces}}\Delta t\left(T_{\alpha,ff,ij}\frac{k_{r\alpha}}{\mu_\alpha}\rho_\alpha\Delta\Phi_{\alpha,ff,ij}\right)^{n+1}-$$

$$\sum_{j=1}^{n_{fF}}\Delta t\left(T_{\alpha,fF,ij}\frac{k_{r\alpha}}{\mu_\alpha}\rho_\alpha\Delta\Phi_{\alpha,fF,ij}\right)^{n+1}=0 \quad (3.35)$$

Where $\phi_{f,i}^{*}$ is the fluid fraction of natural fracture continuum i, n_{faces} is the number of natural fractures j neighboring to the natural fracture continuum i, n_{fF} is the number of connections between natural fracture i and hydraulic fracture j $T_{\alpha,ff,ij}$ is the transmissibility between natural fractures i and j, $T_{\alpha,fF,ij}$ is the transmissibility between the natural fracture i and the hydraulic fractures j. $\Delta\Phi_{\alpha,ff,ij}$ is potential differences of the natural fracture i and natural fracture j. $\Delta\Phi_{\alpha,fF,ij}$ is the potential differences of the natural fracture i and hydraulic fracture j.

For each hydraulic segment i, we assume fluid flow happens between itself and its neighboring hydraulic segment and between itself and natural fractures.

$$\left(V_iS_{\alpha,i}\rho_{\alpha,i}\phi_{F,i}\right)^{n+1}-\left(V_iS_{\alpha,i}\rho_{\alpha,i}\phi_{F,i}\right)^{n}+\sum_{j=1}^{n_{FF}}\Delta t\left(T_{\alpha,FF,ij}\frac{k_{r\alpha}}{\mu_\alpha}\rho_\alpha\Delta\Phi_{\alpha,FF,ij}\right)^{n+1}+$$

$$\Delta t\left(T_{\alpha,fF,ij}\frac{k_{r\alpha}}{\mu_\alpha}\rho_\alpha\Delta\Phi_{\alpha,fF,ij}\right)^{n+1}=0 \quad (3.36)$$

Where $\phi_{F,i}$ is the porosity of the hydraulic fracture which is constant in this thesis, $T_{\alpha,FF,ij}$ is the transmissibility between each hydraulic segment i and j. $\Delta\Phi_{\alpha,FF,ij}$ is the potential difference between each hydraulic segment i and j.

3.6 Solution Algorithm

Methods of coupling between reservoir flow and solid deformation found in the literature can be classified into four different types, fully coupling, iterative coupling and explicit coupling (Tran and Settari, 2004). Now, we review these three coupling methods

1. Iterative coupled: This approach solves flow and geomechanics variables iteratively within a time step until a desired accuracy is reached. For coupled geomechanics and flow, there are two schemes: drained split and undrained split. In drained split scheme, pore pressure is frozen during mechanical solve. In undrained split scheme, when mechanics deformation is being calculated, fluid mass content is fixed, which means fluid is not allowed to flow out of or into the system. Iterative coupled method features flexibility and modularity because different linear solvers could be designed according to the pattern of the matrix in each problem. However, sometimes iterative coupled method could cause numerical instability when rock tends to increase in volume with a reduction in pore pressure (e.g., owing to dilation during shearing) (Gutierrez et al., 2001).

2. Fully coupled: This approach solves flow variables such as pressure, saturation, temperature and geomechanics response such as displacement at once in a Newton's method. Fully coupled system has unconditional stability. Compared to iterative coupled method, it solves a bigger Jacobian matrix at every Newton iteration.

3. Explicit coupling: it is sometimes also called one-way coupling. In this coupling, information is only transferred from a flow simulator to geomechanics simulator, which means changes in fluid pressure affect changes in stress and strain field, stress and strain field changes do not affect fluid pressure yet (Tran and Settari, 2004).

In this study, we use a mixed-space discretization. Finite volume method is applied to fluid flow in which pressure is at the center of the grid block. XFEM is used for poromechanics where displacement vector is located at the vertices.

The final linear system that is solved for coupled geomechanics and flow is written as a compact 3×3 matrix:

$$\begin{pmatrix} A_{pp} & C_{ps} & C_{pu} \\ C_{sp} & A_{ss} & C_{su} \\ C_{up} & C_{us} & K_{uu} \end{pmatrix} \begin{pmatrix} p \\ s \\ u \end{pmatrix} = \begin{pmatrix} F_p \\ F_s \\ F_u \end{pmatrix} \tag{3.37}$$

Where p, s, u are the pressure, saturation and displacement vectors. In the 3 by 3 matrix, each term is the coupling coefficient sub matrix between different items (p, s, u). We solve for the coupled system using fully coupled method.

CHAPTER 4

Numerical Cases

4.1 Mandel's Problem

Abousleiman et al. (1996) presented the canonical example of nonmonotonic behavior in pore pressure following undrained loading. In **Fig. 4.1**, A rectangular plate, length $2a$, width $2b$, is sandwiched between two rigid, impermeable plates. A compressive force F is applied at time zero and then held constant. F is force per unit length in z direction. Fluid pressure is constant at left and right boundary. Because of the symmetric of the domain, only one quarter of the plate is analyzed.

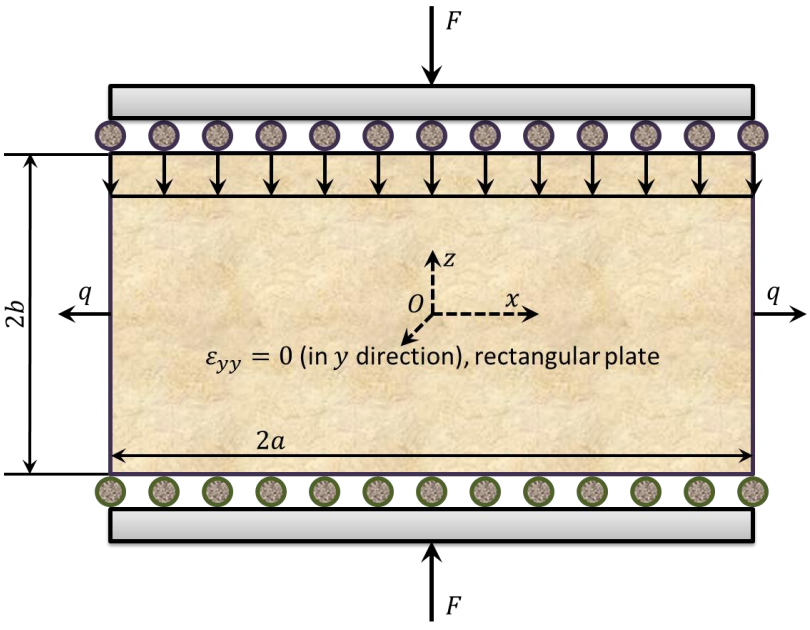

Figure 4.1 Illustration of Mandel's problem

The analytical solution for pore pressure is given as the following (Abousleiman et al., 1996)

$$p = \frac{2FB(1+v_u)}{3a}\sum_{i=1}^{\infty}\frac{\sin\beta_i}{\beta_i-\sin\beta_i\cos\beta_i}\left(\cos\frac{\beta_i x}{a}-\cos\beta_i\right)\exp\left(-\frac{\beta_i^2 ct}{a^2}\right) \quad (4.1)$$

And β_i satisfies

$$\tan\beta_i = \frac{(1-v)}{v_u-v}\beta_i \quad (4.2)$$

The Skempton pore pressure coefficient B, undrained Poisson's ratio v_u and diffusivity coefficient c.(Rice, 1976)

$$B = 1-\frac{\phi K(K_s-K_f)}{K_f(K_s-K)+\phi K(K_s-K_f)} \quad (4.3)$$

$$v_u = \frac{3v+B(1-2v)\left(1-\frac{K}{K_s}\right)}{3-B(1-2v)\left(1-\frac{K}{K_s}\right)} \quad (4.4)$$

$$c = \frac{2kB^2G(1-v)(1+v_u)^2}{9\mu_f(1-v_u)(v_u-v)} \quad (4.5)$$

Where K, K_s, K_f are the bulk modulus of the porous media, solid grains and fluid, v is the drained Poisson's ratio.

Table 4.1 gives the dimension of the specimen and its material properties used in the simulation. **Fig. 4.2** shows the pressure distribution along the x axis with time. The pressure in the plate interior first builds up at early time before the entire domain starts to deplete. The numerical solution gives results in agreement with the analytical solution.

Table 4.1. Input Parameter for Mandel's Problem

Input Data	Value	Unit
Grid Size	$50 \times 50 \times 1$	
Plate Size	$200 \times 2 \times 1$	$m \times m$
Porosity	0.2	
Permeability	10^{-13}	m^2
Young's modulus	10^8	Pa
Drained Poisson's ratio	0.2	
Undrained Poisson's ratio	0.4	
Biot's coefficient	1.0	
Overburden F	10^6	Pa

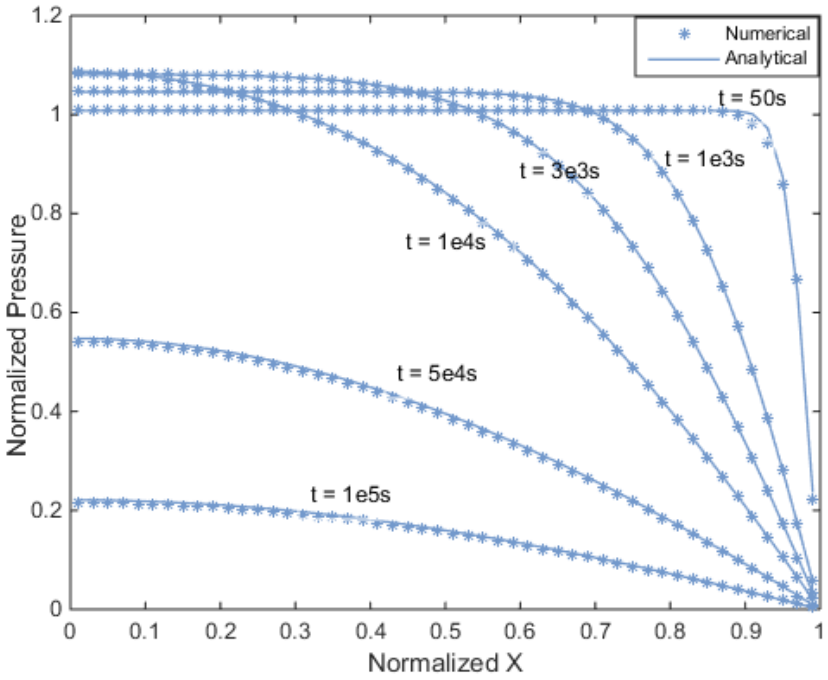

Figure 4.2. Mandel's problem validation

4.2 Single Fracture Mechanics

Stress intensity factor (SIF) is an important parameter for linear elastic fracture mechanics and for assessment of performance of X-FEM (Khoei, 2014). The normalized stress intensity factor is defined as $\overline{K_I} = \frac{K_I}{\sigma\sqrt{\pi a}}$.

First, we have verified our X-FEM by analysis of an infinite plate with a center crack in the domain in Fig. B-1. The exact elasticity solution is used as an input imposed displacement field on the boundaries of a finite plate. Only the right half of the plate is modelled due to symmetry. Four different finite element meshes including 5×10, 10×20, 20×40 and 40×80. The input parameters are $\sigma_\infty = 10^6$Pa, $E = 10^8$Pa, Half Area = 10×20 m^2 , crack half-length $a = 5.35$ m and plane stress condition.

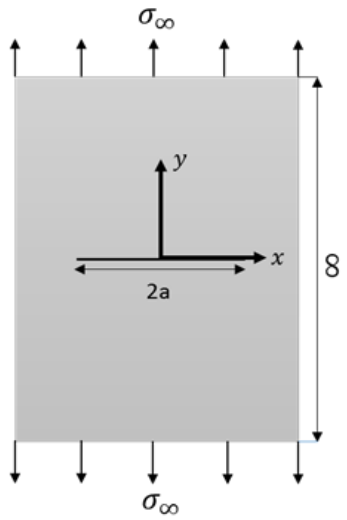

Figure 4.3. Schematic of a center crack in a infinite plane

The analytical solution for crack opening displacement under plane stress condition is given by (Janssen et al., 2006):

$$w = \frac{2\sigma_\infty}{E}\sqrt{a^2 - x^2} \tag{4.6}$$

We compare our numerical results of crack opening displacement (mesh 40×80) with the analytical one and it shows a remarkable agreement with the exact solution.

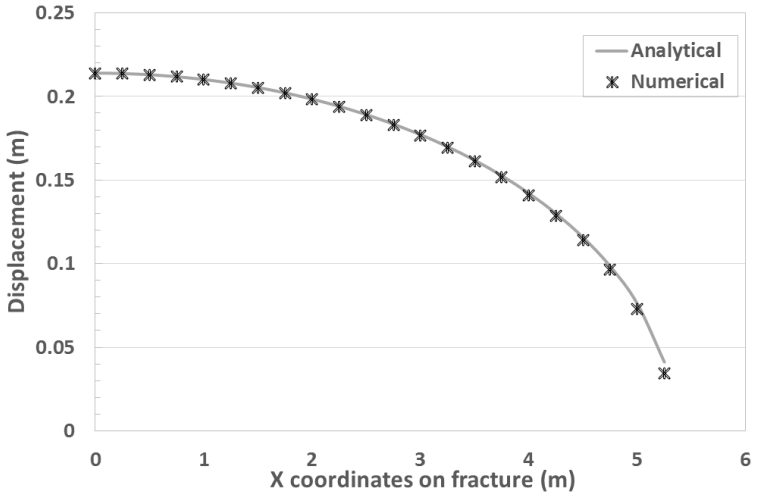

Figure 4.4 Crack opening displacement versus X coordinates on fracture.

Numerical calculation of J integral is to do the following integral (Moës et al., 1999):

$$I^{(1,2)} = \int_A \left[\sigma_{ij}^{(1)} \frac{\partial u_i^{(2)}}{\partial x_1} + \sigma_{ij}^{(2)} \frac{\partial u_i^1}{\partial x_1} - \sigma_{ij}^{(1)} \varepsilon_{ij}^{(2)} \delta_{1j}\right] \frac{\partial q}{\partial x_j} dA \qquad (4.7)$$

Where A is the integral domain which is shown in **Fig. 4.5** (dark grids), A is the grid blocks that are cut by the dashed circle. $\sigma_{ij}^{(1)}$ $u_i^{(1)} are$ the numerical solutions of the stress and displacement near the tip. $\sigma_{ij}^{(2)}, u_i^{(2)}$ are the analytical solutions near the tip which are listed in the Chapter 2. δ_{ij} is the Kronecker delta. $q(\boldsymbol{x})$ is the smoothing weighting function which takes a value of unity on an open set containing the crack tip and vanishes on an outer prescribed dashed circle.

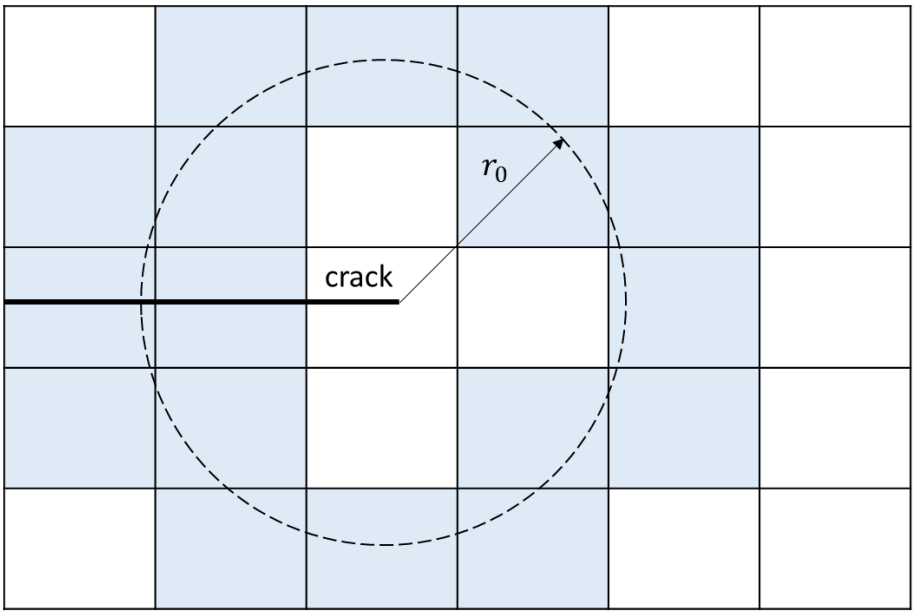

Figure 4.5 Element selected (dark grids) near the crack tip for the J integral

After we calculate the J integral, stress intensity factor K can be calculated by the following equation:

$$K = \frac{2}{E'} I^{(1,2)} \tag{4.8}$$

Where E' is equal to E under plane stress condition and equal to $\frac{E}{1-\nu^2}$ under plane strain condition.

The analytical solution for this problem is $\overline{K_I} = 1$ (Huang et al. 2003). In Table B-1, we do the J-Integral near the crack tip and calculate the numerical result $\overline{K_I}$ which reaches excellent accuracy.

Table 4.2. Normalized values of stress intensity factors

Number of Nodes	Normalized $\overline{K_I}$	Error %
66	1.01449	1.4
231	1.00861	0.86
861	1.0047	0.47
3321	1.0024	0.24

Next, we rotate fracture β degrees from its center counterclockwise. Analytical solution for normalized stress intensify factor has been known as $\overline{K_I} = \cos^2 \beta$.

In Fig. 4.6, it shows the comparison of analytical solution with our numerical results. A remarkable agreement is reached between numerical and analytical values.

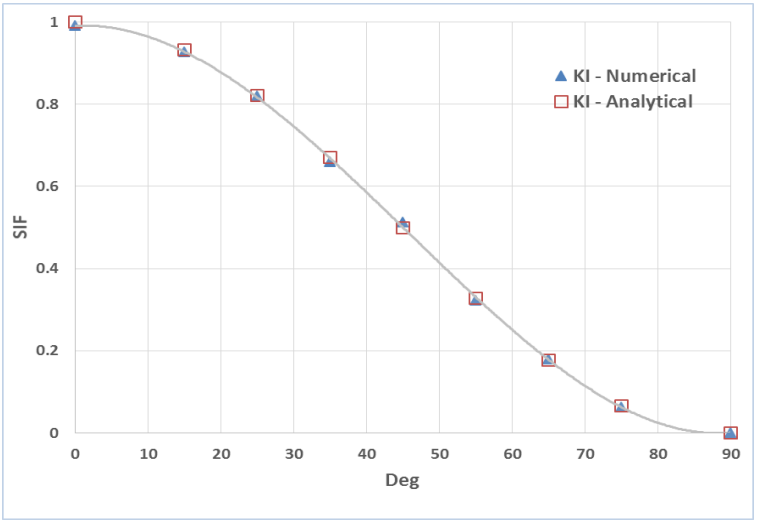

Figure 4.6. Inclined crack stress instensify factor

4.3 Convergence Analysis

We use a XFEM-EDFM simulator without considering dual porosity so that grid refinement can be completed. In **Fig. 4.7**, a central hydraulic fracture in domain is investigated. The boundary of the reservoir is impermeable for fluid flow. On the top and right side of the reservoir, two constant forces are exerted. On the left and bottom side, the displacement are prescribed as zero. Five different number of grid blocks ($25 \times 25, 50 \times 50, 100 \times 100, 200 \times 200, 400 \times 400$) are created to do grid refinement for displacement. Another five different number of grid blocks ($5 \times 5, 15 \times 15, 45 \times 45, 135 \times 135, 405 \times 405$) are created for pressure. The input parameters are listed in Table 4.3.

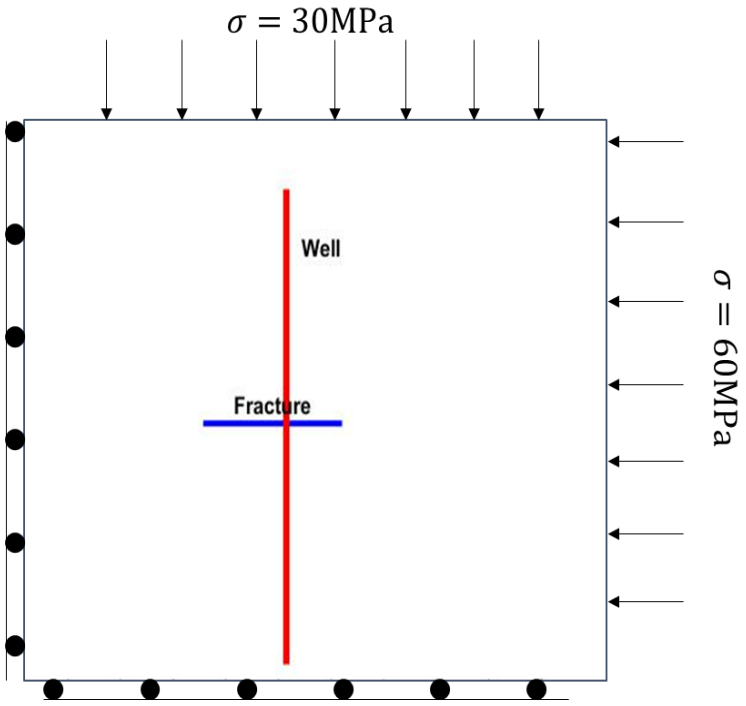

Figure 4.7. A schemeatic of a single hydraulic fracture in the unconventional reservoir

Table 4.3. Parameters for grid refinement.

Input Data	Value	Unit
Reservoir Size	200×200	m × m
Fracture Width	0.005	m
x_f	51	m
ϕ	0.2	
k_m	10^{-18}	m^2
k_{Fi}	10^{-12}	m^2
E_m	50	GPa
v_m	0.2	
α_m	0.8	
E_p	500	MPa
p_i	20	MPa
S_w	0.4	
p_w	5	MPa

Where x_f is the length of the fracture. k_m is the matrix permeability. k_{Fi} is initial hydraulic fracture permeability. E_m is the matrix Young's modulus. v_m is the matrix Poisson ratio. α_m is the matrix Biot's coefficient. E_p is the proppant Young's modulus. p_i is the reservoir initial pressure. S_w is water saturation. p_w is the well pressure.

The coarsest mesh (400×400 for displacement, 405×405 for pressure) in each test is chosen as a reference. The rest are compared to the reference and calculated L2-norm. The error is defined as:

$$\varepsilon = \frac{\sqrt{\sum_{i=1}^{n}(x_i - x_{\text{ref}})^2}}{\sqrt{\sum_{i=1}^{n} x_{\text{ref}}^2}} \tag{4.9}$$

The grid refinement result for pressure and displacement appear on **Fig. 4.8** and **Fig. 4.9**. From the plots, we find that error level of displacement is much smaller than pressure. To reach a good precision, Scale of the mesh should be larger than 100×100.

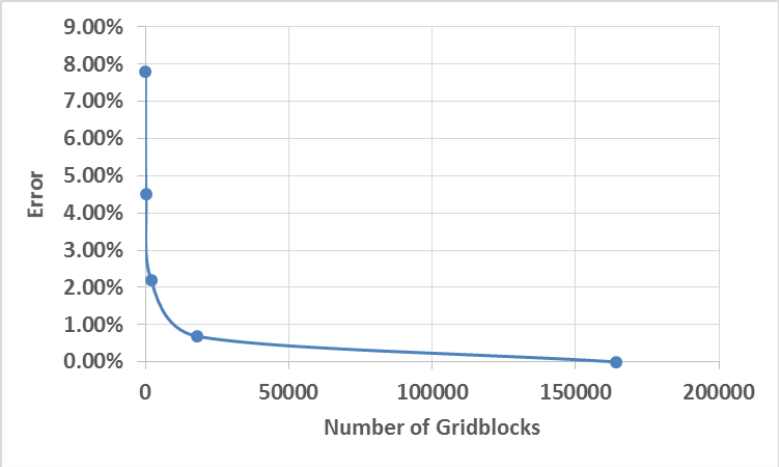

Figure 4.8. Error of pressure versus number of grid blocks

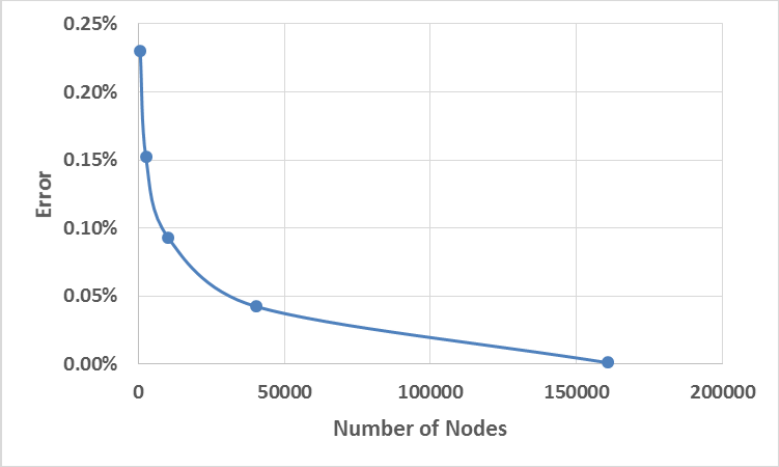

Figure 4.9. Error of displacement versus number of nodes

4.4 Field Examples

We introduce two cases for testing the EDFM-XFEM with dual porosity coupled system. In the following simulation, hydraulic fractures are treated explicitly while natural fractures are assumed as orthogonal continuum which surrounds the matrix continuum.

4.4.1 Effect of Natural Fracture Property on the Coupled System

We introduce a 2D problem with multiple hydraulic fractures as well as dual porosity property for each grid blocks in the domain. The schematic picture is shown in Fig. 8. The reservoir has a length scale of $200\ \mathrm{m} \times 200\ \mathrm{m}$. The domain has 100×100 grid blocks. There is one horizontal well that produces gas and water. The well is intersected with four hydraulic fractures with different length (from down to up,$82, 82, 42, 56\mathrm{m}$). There is no flow on reservoir boundaries. And displacement is fixed on the left and bottom sides of the boundary. Constant force is applied on up and right sides.

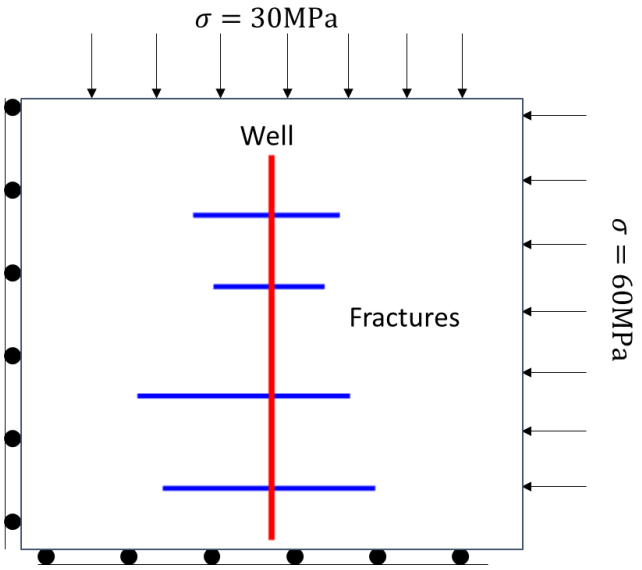

Figure 4.10. A schemeatic of a multiple hydraulic fracture in the unconventional reservoir

For flow, the initial reservoir pressure is $20MPa$ everywhere, initial water saturation S_w is 0.4. Initial permeability and porosity of the fracture continuum are $k_{fi} = 10^{-13}\, m^2$ and $\phi_f = 0.8$. Whereas initial permeability and porosity of the matrix continuum are $k_m = 10^{-18}\, m^2$ and $\phi_m = 0.1$. The initial aperture of natural fractures and hydraulic fractures are $0.001\, m$ and $0.005\, m$ respectively. The well pressure is kept constant at $p_w = 5\ MPa$.

For mechanics, Young's modulus for matrix grain is $E_{\mathrm{m}} = 5\ \mathrm{GPa}$, drained Poisson's ratio is $\nu = 0.2$. In this case, we study on the influence of natural fracture normal stiffness K_n on natural aperture and production rates. Three different natural fracture normal stiffness $K_n = 40$, 60 and 100 $\mathrm{GPa \cdot m^{-1}}$ are investigated. Shear stiffness of natural fracture is fixed at $K_{sh} = 33\ \mathrm{GPa \cdot m^{-1}}$. Young's modulus of proppant is $E_p =$

50 MPa. Biot's coefficient for matrix and natural fractures are $\alpha_m = 0.8$ and $\alpha_f = 0.9$. Plane strain condition is assumed.

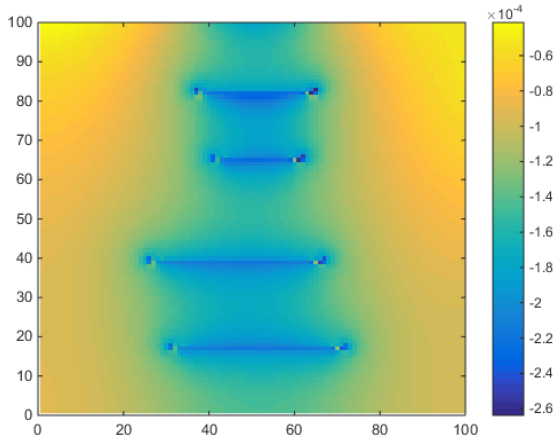

(a)$K_n = 40\ \text{GPa} \cdot \text{m}^{-1}$

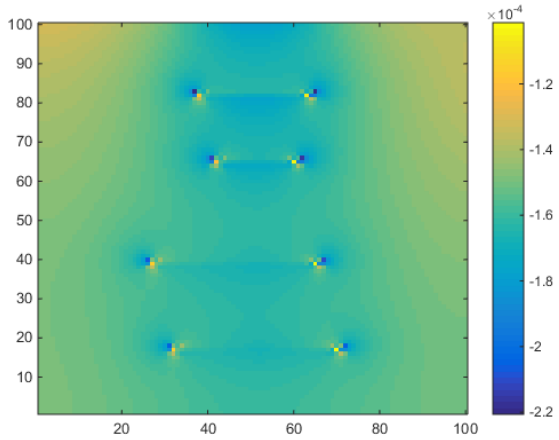

(b)$K_n = 60\ \text{GPa} \cdot \text{m}^{-1}$

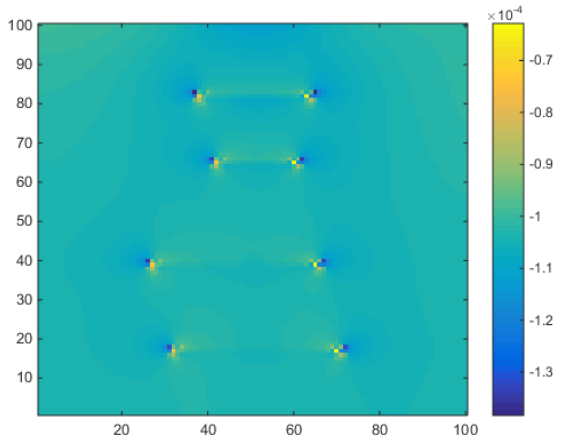

(c)$K_n = 100$ GPa $\cdot$ m^{-1}

Figure 4.11. Natural fracture aperture changes at t $= 200$ days

We plot the natural fracture aperture change in **Fig. 4.11**. The natural fracture aperture change is determined both on external force and pore pressure. We find that when natural fracture normal stiffness K_n increases, the fracture-matrix system becomes stiffer as well. Accordingly, a smaller deformation of natural fracture occurs. It is also shown that natural fracture aperture changes at tips are always larger than other places. It is because stress σ_{yy} at tips tend to be singular for linear fracture, which leads to a larger decrease in natural fracture aperture. Another interesting phenomenon is that there is an obvious contrast of aperture changes between places near well and far away from well at $K_n = 40$ GPa $\cdot$ m^{-1}. While K_n increases, the contrast is fading away. Smaller normal stiffness K_n leads to a larger decrease in natural fracture aperture. As a result, a lower permeability field forms and pressure wave transmit slowly in the reservoir. Accordingly, pressure difference near well and far away from well is larger at $K_n = 40$ GPa $\cdot$ m^{-1} than that at $K_n = 60,\ 100$ GPa $\cdot$ m^{-1}. Therefore, an apparent contrast is observed when $K_n = 40$ GPa $\cdot$ m^{-1}.

In **Fig. 4.12**, we plot gas production rates versus time for three different normal stiffness. The larger normal stiffness K_n, the smaller aperture changes. Therefore a higher permeability field will lead to higher production rates at early days. However, at around $t = 130$ days, production rates of $K_n = 60\text{GPa} \cdot \text{m}^{-1}$ and $K_n = 100\ \text{GPa} \cdot \text{m}^{-1}$become almost the same.

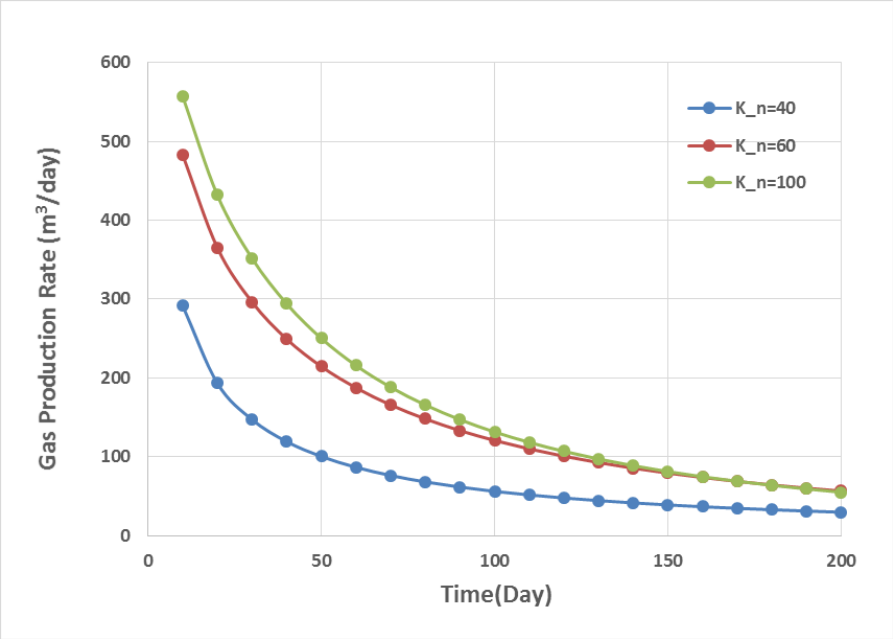

Figure 4.12. Gas production rate versus time

4.4.2 Effect of Proppant Property on the Coupled System

Next, we show an example with varying Young's modulus of proppant and observe its influence on hydraulic fracture aperture and production rates. The hydraulic fracture pattern is changed a little bit. It is shown in **Fig. 4.13**.

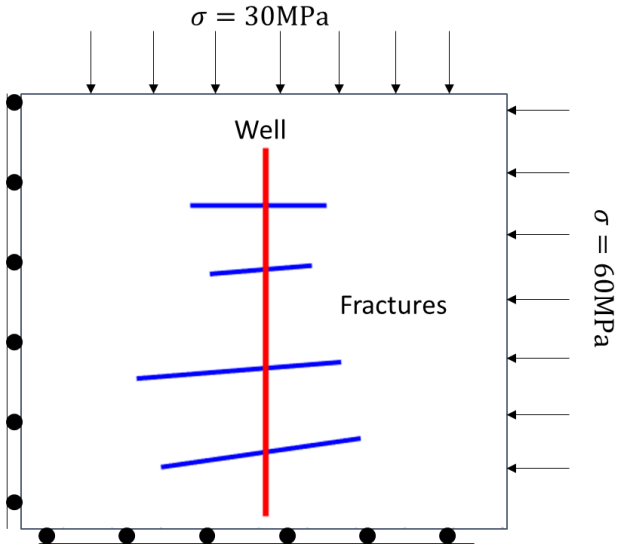

Figure 4.13. A schemeatic of a multiple hydraulic fracture in the unconventional reservoir

In this scenario, we fix the normal stiffness at $K_n = 60\ GPa \cdot m^{-1}$. The Young's modulus of proppant E_p are $10\ MPa$, $50\ MPa$, $500\ MPa$ individually. The remaining parameter values are the same as the last case. The starting and ending points of fracture are listed in the Table 4.4.

Table 4.4. Hydraulic Fracture Position Information

Fracture No	Starting point	Ending point
1	$(61, 33)$	$(141, 47)$
2	$(51, 77)$	$(133, 85)$
3	$(81, 129)$	$(121, 133)$
4	$(73, 163)$	$(127, 163)$

Each hydraulic fracture is intersected with several grid blocks and each intersected segment is called fracture segment. In **Fig. 4.14**, we observe that when proppant becomes stiffer, the hydraulic fracture closes less. The fracture aperture almost does not change along the fracture plane when $E_p = 5E8$ Pa. When $E_p = 5E7$ and $1E7$ Pa, aperture at tip is always larger than at center. It is because along the fracture plane, region around tip is always stiffer than that at center. The stiffer region is more able to stand compaction force from boundary and reduction in pore pressure.

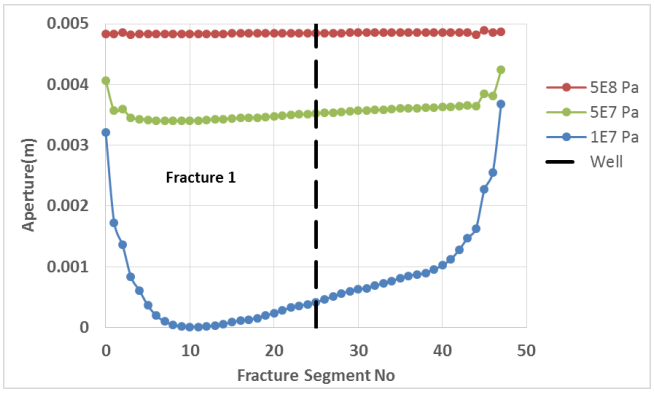
0.005
0.004
0.003
0.002
0.001
0
Aperture(m)
Fracture 1
0
10
20
30
40
50
Fracture Segment No
5E8 Pa
5E7 Pa
1E7 Pa
Well

(a)

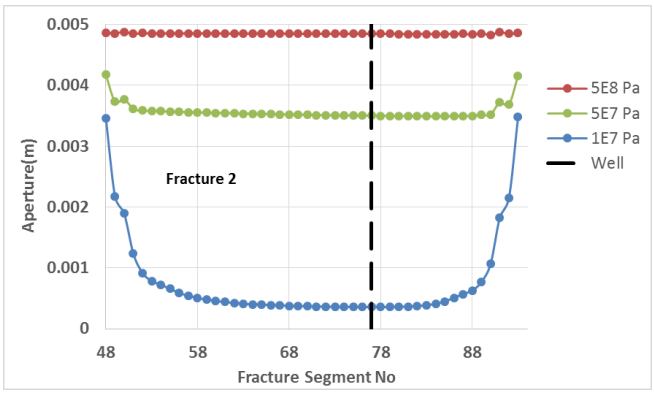
0.005
0.004
0.003
0.002
0.001
0
Aperture(m)
Fracture 2
48
58
68
78
88
Fracture Segment No
5E8 Pa
5E7 Pa
1E7 Pa
Well

(b)

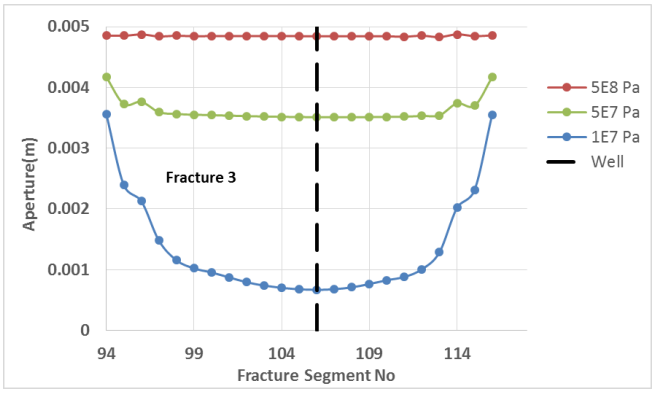
0.005
0.004
0.003
0.002
0.001
0
Aperture(m)
Fracture 3
94
99
104
109
114
Fracture Segment No
5E8 Pa
5E7 Pa
1E7 Pa
Well

(c)

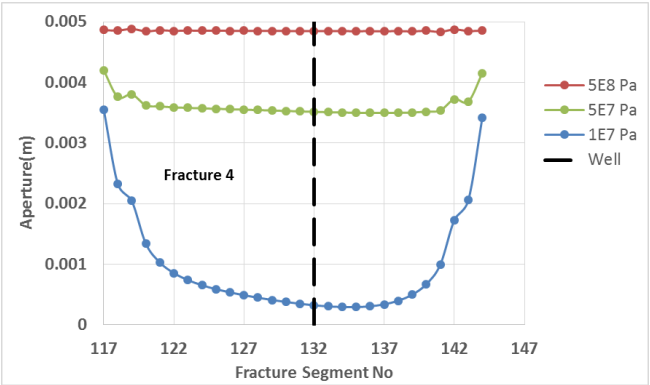

(d)

Figure 4.14. Hydraulic fracture aperture after production for 1000 days. Fracture number is ordered from down to up. Fracture segment number is ordered from left to right and down to up. The black dashed line represents the well that intersects the hydraulic fracture.

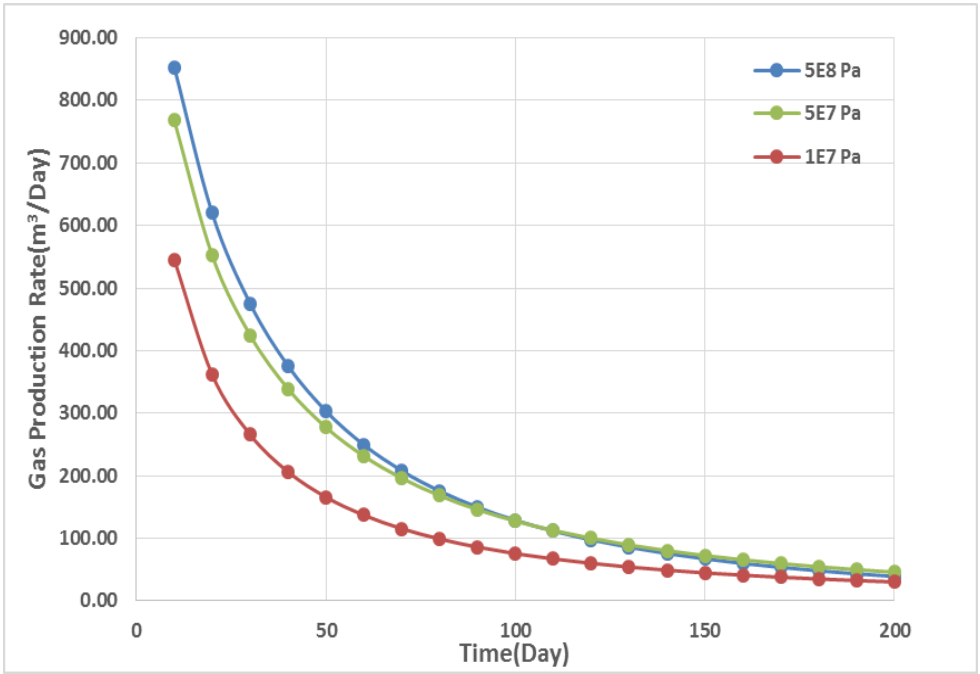

Figure 4.15. Gas production rate versus time

In **Fig. 4.15**, we compare the production rates for the first 200 days. As expectation, the stiffest proppant gives the highest production rates. However, the production rate

differences between $E_p = 5E8$ Pa and $5E7$ Pa are not significantly huge. After 200 days, the production rates tend to be the same for three cases.

CHAPTER 5

CONCLUSIONS

In this work, we develop a fully coupled flow and geomechanics simulator using the combined XFEM-EDFM and dual porosity model approach with fully-implicit time-stepping strategy. A proppant model is proposed to simulate hydraulic fracture production process. The model is validated by available analytical solutions and mesh refinement is performed.

In the case study section, we first investigate the influence of natural fracture norm stiffness on the natural fracture aperture. It shows that a lower normal stiffness causes larger deformation of natural fracture continuum and consequently slow the pressure propagation in the reservoir.

Secondly, we study on the proppant's impact on hydraulic aperture and gas production rates. Results show that stiffer proppant could increase gas production rates. However, only increase in stiffness of proppant may not improve production rates significantly. A less stiff proppant may help achieve a same-level gas production rates.

In future, we recommend to do the following jobs to improve the simulator:

1. Use iterative solvers to solve the linear equation system.
2. Consider fracture contact phenomena in the simulator.
3. Consider hydraulic fracture propagation in the reservoir.
4. Extend the current framework to 3 dimension.

BIBLIOGRAPHY

Abousleiman, Y., Cheng, A.D., Cui, L., Detournay, E. and Roegiers, J.C., 1996. Mandel's problem revisited. Geotechnique, 46(2), pp.187-195.

Azizi, N., Behbahani, R., Isazadeh, M.A., An Efficient Correlation for Calculating Compressibility Factor of Natural Gases, Journal of Natural Gas Chemistry. 19: 642-645, 2010.

Bai, M., 1999. On equivalence of dual-porosity poroelastic parameters.Journal of Geophysical Research: Solid Earth, 104(B5), pp.10461-10466.

Belytschko, T., Moës, N., Usui, S. and Parimi, C., 2001. Arbitrary discontinuities in finite elements. *International Journal for Numerical Methods in Engineering*, *50*(4), pp.993-1013.

Berryman, J.G. and Wang, H.F., 1995. The elastic coefficients of double-porosity models for fluid transport in jointed rock. JOURNAL OF GEOPHYSICAL RESEARCH-ALL SERIES-, 100, pp.24-611.

Berryman, J.G., 2002. Extension of poroelastic analysis to double-porosity materials: New technique in microgeomechanics. Journal of engineering mechanics, 128(8), pp.840-847.

Biot, M. and Willis, D., 1957. The Theory of Consolidation. *J. Appl Elastic Coefficients of the Mech*, *24*, pp.594-601.

Biot, M.A., 1941. General theory of three-dimensional consolidation. Journal of applied physics, 12(2), pp.155-164.

Bourdin, B., Chukwudozie, C.P. and Yoshioka, K., 2012, January. A variational approach to the numerical simulation of hydraulic fracturing. In*SPE Annual Technical Conference and Exhibition*. Society of Petroleum Engineers.

Chen, Z., 2013, May. An ABAQUS implementation of the XFEM for hydraulic fracture problems. In ISRM International Conference for Effective and Sustainable Hydraulic Fracturing. International Society for Rock Mechanics.

Chin, L.Y., Raghavan, R. and Thomas, L.K., 1998, January. Fully-coupled geomechanics and fluid-flow analysis of wells with stress-dependent permeability. In *SPE International Oil and Gas Conference and Exhibition in China*. Society of Petroleum Engineers.

Crouch, S.L., 1976. Solution of plane elasticity problems by the displacement discontinuity method. I. Infinite body solution. *International Journal for Numerical Methods in Engineering*, *10*(2), pp.301-343.

Dolbow, J.E., 1999. *An extended finite element method with discontinuous enrichment for applied mechanics*. Northwestern university.

Fries, T.P. and Belytschko, T., 2010. The extended/generalized finite element method: an overview of the method and its applications.*International Journal for Numerical Methods in Engineering*, *84*(3), pp.253-304.

GUO, J.C., LU, C., ZHAO, J.Z. and WANG, W.Y., 2008. Experimental research on proppant embedment [J]. *Journal of China Coal Society*, *6*, p.017.

Gai, X., Dean, R.H., Wheeler, M.F. and Liu, R., 2003, January. Coupled geomechanical and reservoir modeling on parallel computers. In SPE Reservoir Simulation Symposium. Society of Petroleum Engineers.

Ganis, B., Mear, M.E., Sakhaee-Pour, A., Wheeler, M.F. and Wick, T., 2014. Modeling fluid injection in fractures with a reservoir simulator coupled to a boundary element method. *Computational Geosciences*, *18*(5), pp.613-624.

Garipov, T.T., Karimi-Fard, M. and Tchelepi, H.A., 2014, August. Fully Coupled flow and Geomechanics Model for Fractured Porous Media. In 48th US Rock Mechanics/Geomechanics Symposium. American Rock Mechanics Association.

Gutierrez, M., Lewis, R.W. and Masters, I., 2001. Petroleum reservoir simulation coupling fluid flow and geomechanics. *SPE Reservoir Evaluation & Engineering*, *4*(03), pp.164-172.

Huang, J. and Ghassemi, A., 2012, January. Geomechanical evolution of fractured reservoirs during gas production. In 46th US Rock Mechanics/Geomechanics Symposium. American Rock Mechanics Association.

Huang, R., Sukumar, N. and Prévost, J.H., 2003. Modeling quasi-static crack growth with the extended finite element method Part II: Numerical applications. International Journal of Solids and Structures, 40(26), pp.7539-7552.

Huitt, J.L., McGlothlin, B.B. and McDonald, J.F., 1959, January. The propping of fractures in formations in which propping sand crushes. In*Drilling and Production Practice*. American Petroleum Institute.

Huitt, J.L. and McGlothlin Jr, B.B., 1958, January. The propping of fractures in formations susceptible to propping-sand embedment. In*Drilling and Production Practice*. American Petroleum Institute.

Hajibeygi, H., Karvounis, D., Jenny, P., A hierarchical Fracture Model for the Iterative Multiscale Finite Volume Method, *Journal of Computational Physics*, 2011.

Izadi, G., Wang, S., Elsworth, D., Liu, J., Wu, Y. and Pone, D., 2011. Permeability evolution of fluid-infiltrated coal containing discrete fractures.International Journal of Coal Geology, 85(2), pp.202-211.

Janssen, M., Zuidema, J. and Wanhill, R.J.H., 2006. Fracture mechanics VSSD.

Jha, B. and Juanes, R., 2007. A locally conservative finite element framework for the simulation of coupled flow and reservoir geomechanics.*Acta Geotechnica*, *2*(3), pp.139-153.

Jiang, J. and Younis, R.M., 2015. Numerical study of complex fracture geometries for unconventional gas reservoirs using a discrete fracture-matrix model. Journal of Natural Gas Science and Engineering, 26, pp.1174-1186.

Karimi-Fard, M., Durlofsky, L.J. and Aziz, K., 2003, January. An efficient discrete fracture model applicable for general purpose reservoir simulators. In *SPE Reservoir Simulation Symposium*. Society of Petroleum Engineers.

Khoei, A.R., 2014. Extended finite element method: theory and applications. John Wiley & Sons.

Kim, J., Sonnenthal, E.L. and Rutqvist, J., 2012. Formulation and sequential numerical algorithms of coupled fluid/heat flow and geomechanics for multiple porosity materials. *International Journal for Numerical Methods in Engineering*, *92*(5), pp.425-456.

Kim, J., Sonnenthal, E. and Rutqvist, J., 2015. A sequential implicit algorithm of chemo-thermo-poro-mechanics for fractured geothermal reservoirs. Computers & Geosciences, 76, pp.59-71.

Karimi-fard, M., Firoozabadi, A., Numerical Simulation of Water Injection in Fractured Media Using the Discrete-Fracture Model and the Galerkin Method, *SPE Journal*, 2003.

Kazemi, H., Merrill, L.S., Porterfield, K.L., Zeman, P.R., Numerical Simulation of Water-Oil Flow in Naturally Fractured Reservoirs, *SPEJ*, December 1976.

Lamb, A.R., Gorman, G., Gosselin, O.R. and Onaisi, A., 2010, January. Coupled deformation and fluid flow in fractured porous media using dual permeability and explicitly defined fracture geometry. In SPE EUROPEC/EAGE Annual Conference and Exhibition. Society of Petroleum Engineers.

Lacy, L.L., Rickards, A.R. and Bilden, D.M., 1998. Fracture width and embedment testing in soft reservoir sandstone. *SPE drilling & completion*,*13*(01), pp.25-29.

Levonyan, K., 2011. *Simulation of Coupled Single-phase Flow and Geomechanics in Fractured Porous Media* (Doctoral dissertation, Stanford University).

Liu, J., Chen, Z., Elsworth, D., Miao, X. and Mao, X., 2010. Evaluation of stress-controlled coal swelling processes. International journal of coal geology, 83(4), pp.446-455.

Li, K., Gao, Y., Lyu, Y. and Wang, M., 2015. New Mathematical Models for Calculating Proppant Embedment and Fracture Conductivity. *SPE Journal*,*20*(03), pp.496-507.

Lee, S.H., Lough, M.F., Jensen, C.L., Hierarchical Modeling of Flow in Naturally Fractured Formations with Multiple Length Scales, *Water Resources Research*, 2001.

Li, L., Lee, S.H., Efficient Field-Scale Simulation of Black Oil in a Naturally Fractured Reservoir Through Discrete Fracture Networks and Homogenized Media, *SPEREE*, 2008.

Mindlin, R.D. and Deresiewica, H., 2013. Elastic spheres in contact under varying oblique forces. *Journal of applied mechanics*, *20*.

McClure, M., Babazadeh, M., Shiozawa, S. and Huang, J., 2015, February. Fully coupled hydromechanical simulation of hydraulic fracturing in three-dimensional discrete fracture networks. In *SPE Hydraulic Fracturing Technology Conference*. Society of Petroleum Engineers.

McClure, M.W. and Horne, R.N., 2010, February. Discrete fracture modeling of hydraulic stimulation in enhanced geothermal systems. In *Proceedings of the 35th Workshop on Geothermal Reservoir Engineering*.

Melenk, J.M. and Babuška, I., 1996. The partition of unity finite element method: basic theory and applications. *Computer methods in applied mechanics and engineering*, *139*(1), pp.289-314.

Moës, N., Dolbow, J. and Belytschko, T., 1999. A finite element method for crack growth without remeshing. *International Journal for Numerical Methods in Engineering*, *46*(1), pp.131-150.

Mohammadi, S., 2008. Extended finite element method: for fracture analysis of structures. John Wiley & Sons.

Moinfar, A., Sepehrnoori, K., Johns, R.T. and Varavei, A., 2013, February. Coupled geomechanics and flow simulation for an embedded discrete fracture model. In SPE Reservoir Simulation Symposium. Society of Petroleum Engineers.

Moinfar, A., Varavei, A., Sepehrnoori, K., Johns, R.T., Development of a Coupled Dual Continuum and Discrete Fracture Model for the Simulation of Unconventional Reservoirs, SPE 163647, SPE Reservoir Simulation Symposium, The Woodlands, TX, February 2013.

Monteagudo, J., Rodriguez, A. and Florez, H., 2011. Simulation of flow in discrete deformable fractured porous media. In *SPE Reservoir Simulation Symposium, SPE 141267, The Woodlands, USA.*

Singh, G., Pencheva, G., Kumar, K., Wick, T., Ganis, B. and Wheeler, M.F., 2014, February. Impact of accurate fractured reservoir flow modeling on recovery predictions. In *SPE Hydraulic Fracturing Technology Conference*. Society of Petroleum Engineers.

Terzaghi, K., 1960. From theory to practice in soil mechanics: selections from the writings of K. Terzaghi.

Thomas, L.K., Chin, L.Y., Pierson, R.G. and Sylte, J.E., 2002, January. Coupled geomechanics and reservoir simulation. In SPE Annual Technical Conference and Exhibition. Society of Petroleum Engineers.

Tran, D., Settari, A. and Nghiem, L., 2002, January. New iterative coupling between a reservoir simulator and a geomechanics module. In SPE/ISRM Rock Mechanics Conference. Society of Petroleum Engineers.

Wei, Z. and Zhang, D., 2010. Coupled fluid-flow and geomechanics for triple-porosity/dual-permeability modeling of coalbed methane recovery. International Journal of Rock Mechanics and Mining Sciences, 47(8), pp.1242-1253.

Wick, T., Singh, G. and Wheeler, M.F., 2015. Fluid-Filled Fracture Propagation With a Phase-Field Approach and Coupling to a Reservoir Simulator. SPE Journal.

Wilson, R.K. and Aifantis, E.C., 1982. On the theory of consolidation with double porosity. International Journal of Engineering Science, 20(9), pp.1009-1035.

Wu, K. and Olson, J.E., 2015. Simultaneous multifracture treatments: fully coupled fluid flow and fracture mechanics for horizontal wells. *SPE Journal*,*20*(02), pp.337-346.

Warren, J.E. and Root, P.J., 1963. The behavior of naturally fractured reservoirs. *Society of Petroleum Engineers Journal*, *3*(03), pp.245-255.

Volk, L.J., Raible, C.J., Carroll, H.B. and Spears, J.S., 1981, January. Embedment of high strength proppant into low-permeability reservoir rock. In *SPE/DOE Low Permeability Gas Reservoirs Symposium*. Society of Petroleum Engineers.